



# Influence of early/mid-Holocene climate change and sea level rise on a coast with barrier islands, Rio de Janeiro State, SE Brazil

Fabrício Leandro Damasceno<sup>1,5</sup> · Alves Martins Maria Virgínia<sup>1,2</sup> · Josefa Varela Guerra<sup>3</sup> · Antonio Tadeu dos Reis<sup>3</sup> · Murilo Barros Saibro<sup>1</sup> · Layla Cristine da Silva<sup>1</sup> · Amanda Pacheco Seixas<sup>1</sup> · Vahideh Farhangi<sup>1</sup> · Karina Ferreira Chueng<sup>1</sup> · Miguel Ângelo Mane<sup>1</sup> · Rubens Cesar Lopes Figueira<sup>4</sup> · Mauro Geraldés<sup>1</sup>

Received: 17 November 2023 / Revised: 20 January 2024 / Accepted: 5 February 2024  
© The Author(s) 2024

## Abstract

This work aims to identify the influence of climate change on sedimentary processes associated with the usual regression process during the rise of sea level in the early/middle Holocene in southeastern Brazil. The studied area is on the eastern side of Marambaia Barrier Island, which borders the eastern side of Sepetiba Bay (Rio de Janeiro State, SE Brazil). Nowadays, the Marambaia Barrier Island, a  $\approx 40$  km long and  $\approx 5$  km wide sandy ridge, shields Sepetiba Bay from the direct influence of the Atlantic Ocean. To achieve this goal, grain size, geochemical data (including elemental and stable isotopes), and radiocarbon dating data from sediment core SP10 (spanning depths from 8.2 to 45.5 m), collected in the eastern sector of the Marambaia Barrier Island were analyzed. Core SP10 predominantly consists of sandy sediments with some textural variations. However, Sr/Ba ratios suggest that brackish waters primarily influenced the depositional environment, which was also subject to cyclical marine incursions. The essentially felsic sediments of the interval between 45 and 41 m ( $\approx 10.0$ – $8.5$  ka BP) were probably deposited in a protected tidal plain estuary with mangroves. They were possibly mainly sourced from the nearby Pedra Branca Complex. Subsequently, between  $\approx 41$  and 11 m, the marine influence and hydrodynamics increased, and the sediments exhibited a more mafic mineralogical composition resulting probably from the erosion of the Rio Negro Complex, which is mainly found in the northern region of Sepetiba Bay. The mafic component likely reached the study area through coastal drift connected with Sepetiba Bay. During the drought period, recorded between  $\sim 7.5$  and 7.0 ka cal BP (section 25–21 m), the contribution of the mafic component from the Rio Negro Complex decreased and less weathered sediments were accumulated. On the other hand, marine incursions into the study area became more prominent. During the drier climate phase recorded in the interval  $\approx 11$ – $9$  m (after  $\approx 4.0$  ka BP), the La/Sc values indicate that the sediment included a higher proportion of felsic particles, probably due to more significant restrictions on the connection of the study area with Sepetiba Bay due to the development of the Marambaia Barrier Island. These findings are significant as they demonstrate the influence of geomorphology, climate change, sea level, and the development of Holocene barrier islands on the sedimentation in coastal regions.

**Keywords** Sediment source · Sedimentary environment · Isotopic proxies · Marambaia Barrier Island · Sepetiba Bay

## 1 Introduction

The geological and geomorphological evolution of various coastal ecosystems, including estuaries, bays, lagoons, coastal plains, and deltas, is controlled by three key factors: sediment supply, physical regimes, and sea level oscillations (Alexandrakis et al., 2021; Idier et al., 2019; Laignel et al., 2023). Continental zones contribute significantly to

the sediment supply deposited in marine environments, primarily through fluvial transport (Hay, 1998; Walling, 2006).

Understanding the evolution of transitional marine environments concerning climatic variations and sea level changes is crucial. Demographic data indicate that one-third of the world's population lives within 100 km of the coastline (Reimann et al., 2023) and is directly impacted by geomorphological changes in coastal regions (Walling, 2006). Consequently, environments such as bays, coastal lagoons, estuaries, and deltas have garnered increasing

Extended author information available on the last page of the article

attention from academics globally, including studies in Brazil (Silva et al., 2022). These studies aim to analyze the behavior of sedimentary cover concerning current or past coastal dynamics and the natural and anthropogenic impacts on these systems.

The geomorphology of the coastal region is strongly influenced by the area's topography and geology, sedimentary dynamics, relative sea level oscillations, and coastal hydrodynamics (waves, tides, currents) (Roy et al., 1994). Studies by Rodriguez et al. (2005) have demonstrated that Holocene sea level oscillations led to the formation of barrier islands and paleochannel systems in certain coastal regions. Barrier islands are unconsolidated sandy sediment structures formed under wave action, primarily composed of sands and located in coastal environments. They act as a physical (sedimentary) barrier between the ocean and the continent (Hesp & Short, 1999). As they have a topography just above sea level, barrier islands are environments vulnerable to relative sea level variations (Oertel, 1985), covering  $\approx 15\%$  of the world's oceanic coastline (Davies, 1980).

According to Kraft and John (1979), coastal barrier island systems' sedimentary and morphological characteristics depend on climate, amount of sediment sourced and grain size, wave and tidal behavior, topography, and tectonic and eustatic variations in relative sea level. The interaction of these factors results in different stratigraphic patterns, producing transgressive and regressive barriers (Kraft & John, 1979). Galloway and Hobday (1983) classify three types of barrier island system evolution processes: (a) aggradational, when the rate of sediment supply is equivalent to the rate of creation of sediment compartment space; (b) transgressive, when the sediment supply is less than the sediment accommodation space; and (c) regressive when the sediment rate supply is greater than the sediment accommodation space.

In Brazil, barrier islands are found in states like Rio Grande do Norte (Potiguar Basin), São Paulo (Ilha Comprida), and Rio de Janeiro (Marambaia Barrier Island, also known as Restinga da Marambaia), among others (Carvalho et al., 2020). Marambaia Barrier Island, located in Rio de Janeiro State, Southeast Brazil (Fig. 1), is a sandy ridge approximately 40 km long, with a maximum width of 5 km (Fig. 1). This structure evolved throughout the Holocene, initially under normal regression conditions during sea level rise and then (since  $\sim 5.8$  ka BP) by forced regression when the sea level dropped to its current position (Dadalto et al., 2022; Friederichs et al., 2013).

The development of Marambaia Barrier Island shielded Sepetiba Bay from open ocean processes, transforming it into a semi-confined environment with brackish waters. However, it is known that the Marambaia Barrier Island is a fragile sedimentary structure that has ruptured several times, exposing Sepetiba Bay to coastal erosion processes (Friederichs et al., 2013). Therefore, it is essential to analyze

the sedimentary dynamics processes that led to the establishment of Marambaia Barrier Island to understand the formation of this sandy ridge. Despite some studies on the sedimentary structure of Marambaia Barrier Island, such as Friederichs et al. (2013) and Dadalto et al. (2022), the sedimentary framework of its eastern sector remains virtually unknown.

This study aims to identify the influence of climate change on sedimentary processes during the normal regression process that occurred in the early/middle Holocene in southeastern Brazil. The region studied is on the eastern side of Marambaia Barrier Island, which borders the eastern tip of Sepetiba Bay (Rio de Janeiro State, SE Brazil). The research is based on the analysis of core SP10 collected in the eastern sector of Marambaia Barrier Island (Fig. 1).

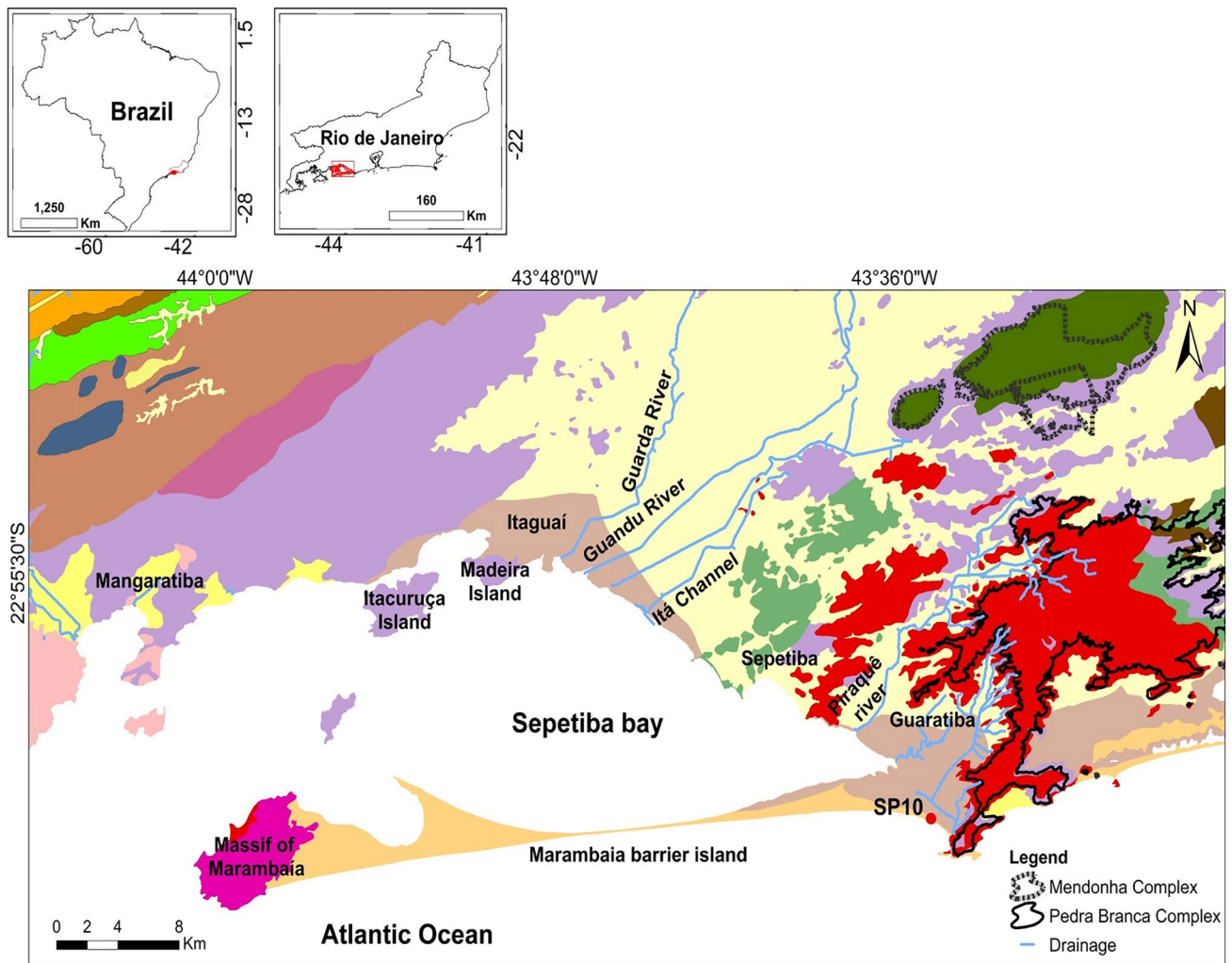
## 2 Study area

Marambaia Barrier Island is situated to the south of Sepetiba Bay (SB) between latitudes  $22^{\circ}53'$  and  $23^{\circ}05'S$  and longitudes  $44^{\circ}01'$  and  $43^{\circ}33'W$  (in the western region of the State of Rio de Janeiro, Southeast Brazil (Fig. 1). Sepetiba Bay with an area of approximately  $450 \text{ km}^2$ , displays an elongated configuration featuring numerous islands and connecting to the South Atlantic Ocean in its western part, as well as to the eastern part of Marambaia Barrier Island through the tidal channels of Barra de Guaratiba.

The region's bedrock, which most influences sedimentation, is predominantly composed of igneous and metamorphic rocks, such as granites, migmatites, gneisses, tonalites, and granodiorites (Heilbron & Machado, 2003) formed during the Neoproterozoic (Tupinambá et al., 2000). A dense drainage network intersects these rocks.

The hydrographic basin surrounding the region has two origins: the slope of the Serra do Mar and the vast lowland area, comprising several rivers, a total of 22 sub-basins, with the Guandu River basin being the primary one (Saucedo-Ramírez et al., 2022). The Guandu River basin is the primary source of siliciclastic sediments, traversing Precambrian rocks, such as migmatites, gneisses, and gneiss-granitoids, and coastal massifs of Marambaia Island, Pedra Branca and Mendanha (with alkaline rocks), Cretaceous dykes, Quaternary fluvial, and fluviomarine deposits (Fig. 1).

The Pedra Branca Complex stands out in the study area as the source of sediments transported to the coast by various rivers flowing into the region. The primary rocks in the Pedra Branca Complex consist of bedded leucogranites with monzogranites rich mainly in quartz, plagioclase (especially microcline), and, to a lesser extent, biotite, apatite, and zircon (Porto Jr. et al., 2018). Additionally, tonalites and granodiorites are rich in quartz, biotite, and plagioclase (Heilbron & Machado, 2003).



- Suruí(su) suite: Leucogranite foliated to biotite, with variations for pegmatoid and porphyritic facies
- Nova Friburgo Suite (nf)- Equigranular to porphyritic granite, leucogranite, Hornblende granodiorite
- Alkaline Complexes: Rocks: nepheline syenite
- Rio Negro Complex: Hornblende orthogneisses, metadiorites, metagranitoids; Gabbro
- Anathetic Syn-Collisional Granitoids: Leucogneisses
- Syn- Collisional Intrusive or Hybrid Granitoids-Biotite foliated porphyritic granite
- Late-Collisional Granitoids: Hornblende-biotite granitic to granodioritic gneiss
- Arcadia Unit - Sand-garnet-biotite banded gneisses, with intercalations of quartzites, calcisilicate rocks
- Conservation Unit - garnet-biotite gneiss; sillimanite-garnet-biotite banded gneiss, N migmatitic
- Kinzigite: Cordierite, graphite and sillimanite. Garnet-biotite gneiss
- Orthogranulites of varying composition, including charnockite and gabbroic rocks
- Alluvial deposits- Sand bars, floodplain and channel filling
- Coastal deposits - Sand with marine shells and well-sorted fine sand dunes
- Swamp and mangrove deposits- Clay, peat, silt, sediment
- Fluvial-marine deposits - Indiscriminate deposits of swamps and mangroves, fluvio-lagoons

**Fig. 1** Location map of the study area with the location of core SP10, including the Guandu River Basin Modified from the Geological Map of the Rio de Janeiro State published by the CPRM (2001)

Marambaia Barrier Island exhibits a variety of morphological and sedimentary domains. It displays, particularly in its eastern sector, coastal sandy ridges, bundles facing the bay, and the tidal plain with mangrove development (Dadalto et al., 2022).

In the contemporary scenario, the study area boasts a great diversity of environments, including sandy beaches (with medium to coarse sands), flooded areas, either colonized by mangroves or not, and tidal channels where medium sands to fine sediments predominate (Carvalho & Guerra, 2020). The eastern limit of the Marambaia Barrier Island is an inlet (Barra de Guaratiba Channel) approximately 4 m deep, covered by medium sands, where tidal currents velocities exceed 2 m/s (Carvalho & Guerra, 2020). In contrast to other channels identified in seismic records, the position of the Barra de Guaratiba Channel remains fixed due to a rocky coastline.

### 3 Materials and methods

Core SP10 was collected using a rotary drilling rig (Sondec SS61) in 2017 on the eastern sector of the Marambaia Barrier Island (latitude 23°03'16.1 S, longitude 43°34'43.0 W), near the Centro de Avaliação do Exército (Army Evaluation Center; CAEX; Fig. 1). After drilling, 1.5 m long tubes were extracted, identified (with the section number and indication of the top and bottom) and sent to the Petrophysics Laboratory of the Fluminense Federal University (LAGEMAR/UFF). This study focuses on the interval between 8.2 and 45.5 m (the initial 8.2 m of sediment could not be recovered). Hence, the top of the analyzed section is considered the 8.2 m level, and the base is the 45.5 m level.

The tubes were opened, and the sediment was sectioned at 10-cm intervals. During this processing stage, materials that could be dated by  $^{14}\text{C}$  (shells and wood fragments) were selected. The 102 obtained samples underwent textural analysis, with 50 sediment layers selected for elemental geochemical analysis and 14 sediment layers (obtained in the finest and richer organic matter (OM) section, between 45.5 and 34.0 m) for stable isotopic analysis in organic matter.

The samples selected for textural analysis were oven-dried, homogenized, quartered, and weighed (initial weight of  $\approx 100$  g of sediment). Subsequently, the samples were oxidized using hydrogen peroxide ( $\text{H}_2\text{O}_2$ ), and carbonates ( $\text{CaCO}_3$ ) were removed with hydrochloric acid (HCl). These procedures were interspersed with washing sessions, oven drying at an average temperature of 55 °C, and weighing on an analytical balance. The percentage of organic matter (OM) and carbonates were determined by dry weight difference after the described procedures.

The coarse and fine fractions of the sediment were separated through wet sieving (with distilled water) using a

63- $\mu\text{m}$  sieve. Once separated, both fractions were oven-dried at 50 °C. The coarse fraction underwent further separation by dry sieving using a set of 9 sieves: < 2000  $\mu\text{m}$ , 1000  $\mu\text{m}$ , 500  $\mu\text{m}$ , 355  $\mu\text{m}$ , 250  $\mu\text{m}$ , 180  $\mu\text{m}$ , 125  $\mu\text{m}$ , 90  $\mu\text{m}$ , and 63  $\mu\text{m}$ . Each sample was subjected to a mechanical shaker for 20 min with a vibration intensity of 8. The sediment retained on each sieve was weighed on an analytical balance and subsequent statistical analysis. Particle size analyses were conducted at the Geological Oceanography Laboratory of Universidade do Estado do Rio de Janeiro (LaboGeo-UERJ). The textural parameters were determined according to Folk and Ward (1957).

### 3.1 Elemental geochemical analysis

For the elemental geochemical analysis, the selected samples of total sediment underwent grinding in an agate mortar and subsequently sieved through a 63  $\mu\text{m}$  sieve. The resulting powdered sediment was subjected to total digestion with four acids ( $\text{HNO}_3$ ,  $\text{HClO}_4$ , HF, and HCl) and analyzed through Inductively Coupled Plasma Atomic Emission Spectrometry (ICP-AES) at the Bureau Veritas Ltd laboratory, Vancouver (Canada). Thirty-five chemical elements were analyzed in 50 sediment samples distributed along the core. The geochemical results estimated the concentrations of specific oxides, including  $\text{Al}_2\text{O}_3$ , CaO, FeO,  $\text{K}_2\text{O}$ , MgO, MnO,  $\text{Na}_2\text{O}$ ,  $\text{TiO}_2$ , and  $\text{Fe}_2\text{O}_3$ .

Additionally, various ratios were applied to represent changes in the geochemical composition of the sediments, such as Ti/Ca, considered an indicator of terrigenous input (Arz et al., 1998; Govin et al., 2012); Y/Ni, Cr/V, La/Sc and Th/Co, Th/Sc, to indicate changes in the sources of lithogenic materials in the study area (Bhatia & Crook, 1986; Cullers, 2002; Okunlola & Idowu, 2012); Sr/Ba to distinguish marine and terrestrial sedimentary environments (Wang et al., 2021; Yan et al., 2021); Ti/Zr to understand weathering processes and also to indicate homogeneity/discontinuity of source materials (Dress & Wilding, 1973; Montibeller et al., 2017).

In addition, the V/Cr was used to identify changes in redox conditions (Jones & Manning, 1994; Powell et al., 2003). This ratio has been widely used in the literature to indicate redox conditions (e.g., Rimmer, 2004; Tabatabaei et al., 2012). The boundary between an oxic–dysoxic and dysoxic–anoxic environment was considered between 2 and 4.25 for V/Cr, as suggested by Jones and Manning (1994).

### 3.2 Geochemical indices

Geochemical indices were used to assess the weathering of the source rocks. The ICV, CIA, and PIA indices (calculated as shown below) have been used to detect variations in paleo-weathering as demonstrated by several studies (e.g.,

Armstrong-Altrin et al., 2017; Bela et al., 2023; Nguetchoua et al., 2019). These indices were formulated based on the assumption that the intensity of chemical weathering influences the mineralogical composition of the sediments deposited in a basin.

The Index of Compositional Variability (ICV) was determined according to Cox et al. (1995), measuring the relative abundance of aluminum versus other major cations in a rock or mineral. The ICV was calculated using the equation:  $ICV = (Fe_2O_3 + K_2O + Na_2O + CaO + MgO + MnO + TiO_2) / Al_2O_3$ . The ICV index compares the alumina concentration in the sample, common in clay minerals, with other cations that are more common in other minerals. High ICV values tend to be related to non-clay silicates with a low proportion of  $Al_2O_3$ . Furthermore, Cox et al. (1995) suggested that ICV values are lower in minerals more stable at Goldich's (1938) weathering trend, such as the alkali feldspars. The relationship between weathering resistance and ICV helps identify the sediments' compositional maturity.

The Chemical Alteration Index (CIA), developed by Nesbitt and Young (1984) and McLennan et al. (1993), was also applied in this study to estimate the degree of the sediment's weathering. Nesbitt and Young (1984) used, as a principle, the mineralogical composition of the upper crust and how the respective minerals behave during the chemical weathering process. According to Wedepohl (1969), the upper crust is composed of approximately 21% quartz, 41% plagioclase, and 21% K-feldspar. Nesbitt and Young (1982) suggested that clay minerals are formed synchronously during the degradation of minerals from the feldspar group. During this process, elements such as Ca, Na, and K are removed, and the proportion of Al increases as weathering increases.

CIA indicates the source rock's chemical weathering level based on the minerals present in the sample. The Chemical Alteration Index was calculated using the equation:  $CIA = [Al_2O_3 / (Al_2O_3 + CaO^* + Na_2O + K_2O)] \times 100$ . If the molecular content of CaO is lower than that of  $Na_2O$ , the CaO value is used for  $CaO^*$ ; however, if the opposite occurs, the  $Na_2O$  value is used instead of  $CaO^*$  when calculating the CIA values (Shao et al., 2012).

Another employed index was the Plagioclase index of alteration (PIA), according to Fedo et al. (1995). This index is represented by the equation  $PIA = [Al_2O_3 - K_2O / (Al_2O_3 + CaO^* + Na_2O - K_2O)] \times 100$ . The PIA, derived from the CIA equation, signifies the level of chemical alteration in the sediments based on the presence or absence of clay minerals. As with the CIA calculation, values assigned to  $CaO^*$  are either CaO (if  $CaO < Na_2O$ ) or  $Na_2O$  (if  $CaO > Na_2O$ ).

Values of CIA and PIA  $< 60$  indicate low weathering, between 60 and 80 suggest levels of intermediate chemical weathering, and  $> 80$  indicate high levels of weathering (Fedo et al., 1995; McLennan et al., 1993; Nesbitt & Young,

1984). ICV values  $< 1$  indicate mature sediments with more clay minerals. ICV values  $> 1$  indicate a higher presence of compositionally more immature non-clay siliciclastic minerals (Cox et al., 1995).

The C-value index, developed by Zhao et al. (2007) and Cao et al. (2012), was determined using the equation:  $C\text{-value} = \sum (Fe + Mn + Cr + Ni + V + Co) / \sum (Ca + Mg + Sr + Ba + K + Na)$ . This index was used to infer variations in humidity in the environment. The C-value is based on the premise that chemical elements in the numerator become more abundant in the basin during higher humidity, increasing the ratio value. Conversely, during periods of increased aridity, the ratio tends to decrease due to the high concentration of the chemical elements found in the denominator of the expression.

### 3.3 Isotopic analysis

Approximately 2 g of the total sediment was homogenized and decarbonated by adding an equal amount of HCl acid (1:1 ratio). In this procedure, the samples underwent washing and drying in an oven at 50 °C. For the quantification of  $\delta^{13}C$  data, the Costech Instruments Elemental Combustion equipment, coupled to a Thermo Scientific Delta V Advantage Isotope Mass Spectrometer (EA-IRMS), was used at the Marine Organic Chemistry Laboratory (LabQOM, University of São Paulo, Brazil).

### 3.4 Statistical analysis

Before the statistical analysis, data from the core SP10 were normalized using the natural logarithm transformation ( $\log(x + 1)$ ). Pearson's correlations were computed, and a significance threshold of  $p$  value  $< 0.050$  was applied. Additionally, a principal component analysis (PCA) was conducted to explore the overall relationships between the variables. Only variables with factor loading  $> 0.50$  for the first four PCA factors were included in the analysis. The factor scores for the first four PCA factors were then plotted against depth. The statistical analyses were performed using Statistica 12 software.

### 3.5 Radiocarbon dating

Radiocarbon dating was conducted on two shells and a wood fragment. The analyses were carried out at the Beta Analytic Inc. Laboratory (Miami, USA) using the Accelerator Mass Spectrometry (AMS) method. This method accounts for the count of each atom present in all the carbon isotopes. The samples underwent chemical pre-treatment to eliminate impurities to ensure accuracy. The wood fragment was subjected to the so-called Acid-alkali-acid (AAA) pre-treatment, involving an initial bath in hydrochloric acid (HCl) to

remove carbonates, followed by the removal of organic acids using sodium hydroxide (NaOH) and a final wash with HCl to neutralize it before the drying procedure.

The radiocarbon results for the wood material and shells were calibrated using the SHCAL20 database (Hogg et al., 2020) and the MARINE20 curve (Heaton et al., 2020) for the Southern Hemisphere, respectively. The Bayesian analysis probability method proposed by Bronk Ramsey (2009) was employed to estimate the radiocarbon ages (Bronk Ramsey, 2009). The Delta-R value, specific to the study area, was applied to calibrate the shells, with a value of  $-59 \pm 42$  years, following the methodology outlined by Macario et al. (2018). The ages from this work are referred to in calibrated years before the present (yrs. cal BP) or 1000 years before the present (ka cal BP).

## 4 Results

### 4.1 Radiocarbon dating

The ages determined by carbon-14 dating are presented in Table 1. Based on the radiocarbon results and the interpretations in the discussion section, it can be deduced that the analyzed section covers approximately  $\approx 10$  to  $\approx 4$  ka cal BP. This timeframe corresponds to the Holocene transgression when the sea level reached 1–3 m higher than today, around 5 ka cal BP (Angulo et al., 2006). This period also marks the start of the development of Marambaia Barrier Island (Reis et al., 2020).

### 4.2 Sediment texture

Core SP10 is a predominantly sandy sedimentary sequence (Appendix 1). Within the middle segment (between 36 and 31 m) and the upper segment (between 18 and 12 m) of the core, there is an observable trend of increasing sediment mean grain size (Fig. 2A). The finest fraction is located at the base of the core, particularly in the interval between 41 and 36 m. In the upper and middle sections of the core, the sand fraction prevails, with medium and fine sand fractions being predominant. Coarse sand content increases notably

in the intervals of 35–31 m and 25–21 m. Generally, the core exhibits an ascending trend in sediment grain size from the base up to 18.8 m, followed by a reduction towards the top (Fig. 2A).

The upper and middle sections of the core are primarily unimodal, while the sediments at the core's base exhibit bimodal and polymodal characteristics. The modes comprising the top and middle sections of the core are  $427.5 \mu\text{m}$  and  $152.5 \mu\text{m}$ . In contrast, the modes characterizing the lower section are expressed as  $107.5 \mu\text{m}$ ,  $605 \mu\text{m}$ , and  $76.5 \mu\text{m}$ .

The sediment varies from poorly sorted, with some very poorly sorted levels at the base, to moderately/well sorted towards the top. This transition is evident from the depth of 41 m upwards, where the core ceases to have a significant percentage of fine fraction and becomes predominantly sandy.

Skewness values in most of the core tend to be positive. Negative values are primarily identified in the lower portions of the deposit, between 41 and 36 m. The highest skewness values are observed in the upper part of the core SP10, particularly from 18 m to the top (Appendix 1).

### 4.3 Elemental geochemical results

Organic matter (OM) contents ( $\leq 9.9\%$ ; mean  $1.0 \pm 1.9\%$ ) are generally low (Appendix 2; Fig. 2B). However, they exhibit higher values at the core base. Carbonate contents follow a similar pattern to organic matter at the base of the core (Appendix 1; Fig. 2B). Carbonates also increase in the core's middle section.

The S content was below the detection limit of the equipment in the upper part of the core but tended to increase towards the core base (max.  $3.0\%$ ; Appendix 2; Fig. 2B). Sulfur contents demonstrate a similar distribution pattern to the OM, with the most significant values found at the core base (Fig. 2B).

The values and ranges of the analyzed element concentrations are included in Table 2 and Appendix 2. Aluminum, Fe, and Ca stand out among the analyzed chemical elements, reaching  $14.8\%$ ,  $11.5\%$ , and  $7.5\%$ , respectively (Appendix 2). Among the trace elements, Ba, Mn, and Sr stand out, reaching  $1183 \text{ mg kg}^{-1}$ ,  $1100 \text{ mg kg}^{-1}$ , and  $472 \text{ mg kg}^{-1}$ , respectively (Appendix 2).

In general, Ca, Sr, Ba, and Mg tend to exhibit a similar distribution pattern throughout the core SP10, reaching higher concentrations in the middle section (Appendix 2; Fig. 3A). Similar to carbonates, OM and S, the concentrations of Pb and Zr (Fig. 2B) decrease towards the core top, with more significant levels in the lower portion of the core (Appendix 2).

**Table 1** Radiocarbon dating carried out on the core SP10

Depth (m)	Material	Conventional age (BP)	Calibrated age (Cal BP)
20.0	Shell	$8383 \pm 40$	7016–6624
21.3	Shell	$8713 \pm 40$	7426–7064
26.0	Wood	$8810 \pm 30$	7961–7645

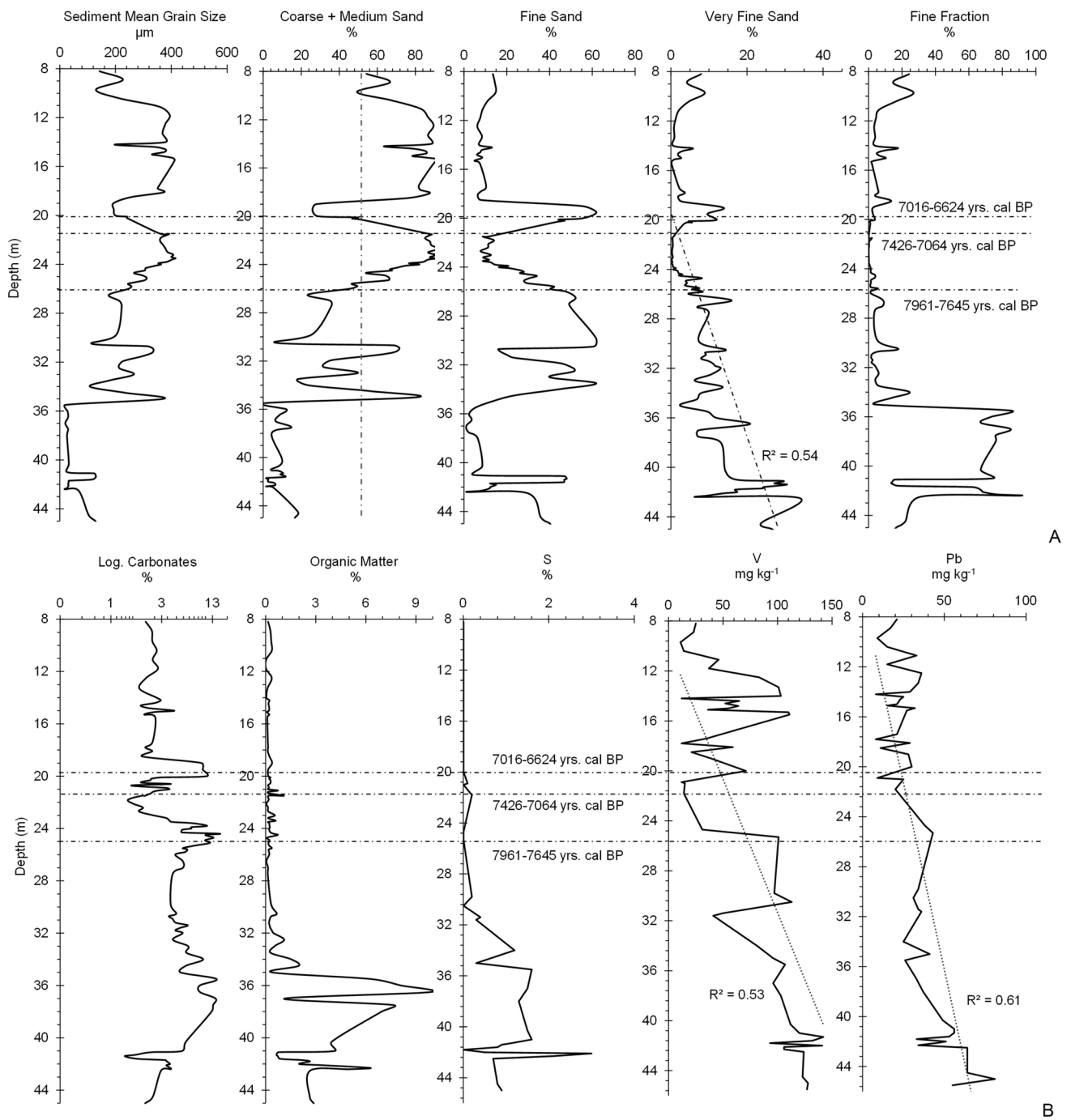


**Fig. 2** Depth plots: **A** sediment mean grain size (μm) and coarse+medium sand, fine sand, very fine sand, and fine fractions (%); **B** carbonates (%), organic matter (%), S (%), V (mg kg<sup>-1</sup>), and Pb (mg kg<sup>-1</sup>) contents. The estimated ages have been signed on the

graphs. The regression lines and the respective  $R^2$  values have been plotted for the very fine sand, V, and Pb contents. The scale for the XX axis of carbonates is logarithmic

The concentrations of Al, Zr, Nb, and the Y/Ni, Th/Co, Ti/Ca, and V/Cr ratios are also higher in the core base and reduce towards the core top (Fig. 3A-C). Although the La/Sc ratio shows significant values at the core base, it also shows significant values at the top (Fig. 3D). The Zr/Sc, Ti/Zr, and

Sr/Ba ratios show several peaks along the core (Fig. 3C). However, the distribution patterns of the Zr/Sc and Ti/Zr values are mainly opposite.

The C-values vary significantly along the core SP10 (0.2–3.5; mean  $1.4 \pm 0.8$ ; Appendix 2, Fig. 4). The CIA,

**Table 2** Maximum, minimum, mean, and standard deviation (Std. dev.) of the concentration of chemical elements along the core SP10

Element		Maximum	Minimum	Mean	Std. dev
Al	%	14.8	1.3	6.8	3.4
Ba	mg kg <sup>-1</sup>	1183	113	463.2	234
Ca	%	7.5	0.1	1.5	1.7
Co	mg kg <sup>-1</sup>	32	...	12.9	8.2
Cr	mg kg <sup>-1</sup>	153	11	70.1	38.8
Fe	%	11.5	0.7	5.2	2.6
K	%	3.8	0.5	1.8	1
La	mg kg <sup>-1</sup>	444	11	85.5	117.4
Mg	%	1.3	0.1	0.6	0.3
Mn	mg kg <sup>-1</sup>	1100	79	519.8	270.6
Mo	mg kg <sup>-1</sup>	20	...	8.8	5.5
Na	%	2.7	0.1	0.6	0.5
Nb	mg kg <sup>-1</sup>	67	4	22.2	17.2
Ni	mg kg <sup>-1</sup>	107	9	40.4	27.5
Pb	mg kg <sup>-1</sup>	81	8	32.8	16.2
S	%	3	...	1	0.7
Sc	mg kg <sup>-1</sup>	18	1	9.5	5.3
Sr	mg kg <sup>-1</sup>	472	44	169.4	114.2
Th	mg kg <sup>-1</sup>	212	...	33.4	58.9
Ti	%	1.7	0.1	0.5	0.4
V	mg kg <sup>-1</sup>	142	11	74.7	42.5
Y	mg kg <sup>-1</sup>	59	4	21.5	15.5
Zr	mg kg <sup>-1</sup>	298	17	79.3	72.5

PIA, and ICV values also showed significant variability (Appendix 2; Fig. 4). The CIA reached a value of 92.4 (mean:  $76.2 \pm 13.1$ ). The highest CIA values were recorded mainly at the core base, between 42 and 35 m, and at the top, between 15 and 11 m. CIA recorded its lowest values at intermediate layers of core SP10, mainly near 21 m and 31 m depth (Fig. 4).

The PIA generally followed the CIA trends. Its maximum value was 97.6 (average:  $85.9 \pm 15.4$ ; Appendix 2) at the core base (Fig. 4). The lowest PIA values, as with the CIA, were identified in the intermediate layers of the core, mainly around the 21 m depth (Fig. 4). The top and bottom of the core have the highest PIA values (Fig. 4).

ICV showed an inverse trend to CIA and PIA (Fig. 4). Its values are mostly  $> 1$  (average:  $1.4 \pm 0.96$ ; Appendix 2). Their highest value was recorded between the depths of 22–19 m (Fig. 4). The lowest ICV values, mostly  $< 1$ , were observed at the core base, mainly between 45 and 42 m depth (Fig. 4).

#### 4.4 Isotopic results in organic matter

The  $\delta^{13}\text{C}$ ,  $\delta^{15}\text{N}$ , and total-N values between 45.5 and 34.0 m, representing the finest and the most organic-rich segment, are included in Table 3. The  $\delta^{13}\text{C}$  values range from -27.30

‰ to -22.43 ‰,  $\delta^{15}\text{N}$  values varied from 8.21 ‰ to 18.42 ‰, and total-N values oscillated between 0.0077% and 0.1717%. The variability of  $\delta^{13}\text{C}$ ,  $\delta^{15}\text{N}$ , and total-N values can be analyzed in Fig. 5A. Figure 5B highlights the inverse relationship between  $\delta^{15}\text{N}$  and total-N values, showing a decrease in total-N values as  $\delta^{15}\text{N}$  values decrease.

#### 4.5 Statistical results

The Biplot comparing Factor 1 to Factor 2 of the PCA (Fig. 6) explains 51.41% and 18.39% of the data variability (totaling 69.8%), respectively. The PCA utilizes the elemental concentrations as active variables and the textural variables as subordinate units (Fig. 6). The analysis reveals that the increase in the concentration of most of the chemical elements correlates with fine fraction and organic matter; the increase in calcium is related to an increase in coarse sediment fractions; sorting and fine particles are opposed to Cr, Mg, Mn, Fe, Ni, and Mo.

Pearson's correlations (shown in Appendix 3) broadly support the PCA results (Fig. 6). They suggest that organic matter positively correlates with fine grain size and most chemical elements, particularly those associated with terrigenous sources, such as Al, Zr, Th, and Ti. Additionally, these parameters are negatively correlated mainly with Ca. Calcium, in turn, positively correlates with other metals such as Ba and Sr. Furthermore, sediment mean grain size (SMGS) and carbonates demonstrate strong positive correlations with Ca, Ba, and Sr.

## 5 Discussion

### 5.1 Sediment source areas

The Y/Ni versus Cr/V diagram (Fig. 7A) suggests that the sediments comprising core SP10 were mainly derived from metamorphic rocks. However, some layers exhibit a relatively more significant contribution of sediments from the erosion of granitic rocks. According to the model proposed by Heilbron et al. (2020), the Sepetiba Bay region is part of the Eastern Terrain, an outer arc system that agglutinated to the São Francisco-Congo paleocontinent between 605 and 595 Ma. This event resulted in high-temperature metamorphism and progressive deformation, generating multiple and varied granitoid plutons. Thus, the region consists of metamorphic rocks, post-collisional granites, and sediments from the Cretaceous and Cenozoic (forearc and back-arc basins).

Regarding the region's geology, the rocks that make up the Eastern Terrain comprise gneisses intercalated with marbles and amphibolites (Italva Group; Peixoto et al., 2017) and high-grade metapelitic paragneisses with quartzite lenses and calcisilic rocks (São Fidelis Group;



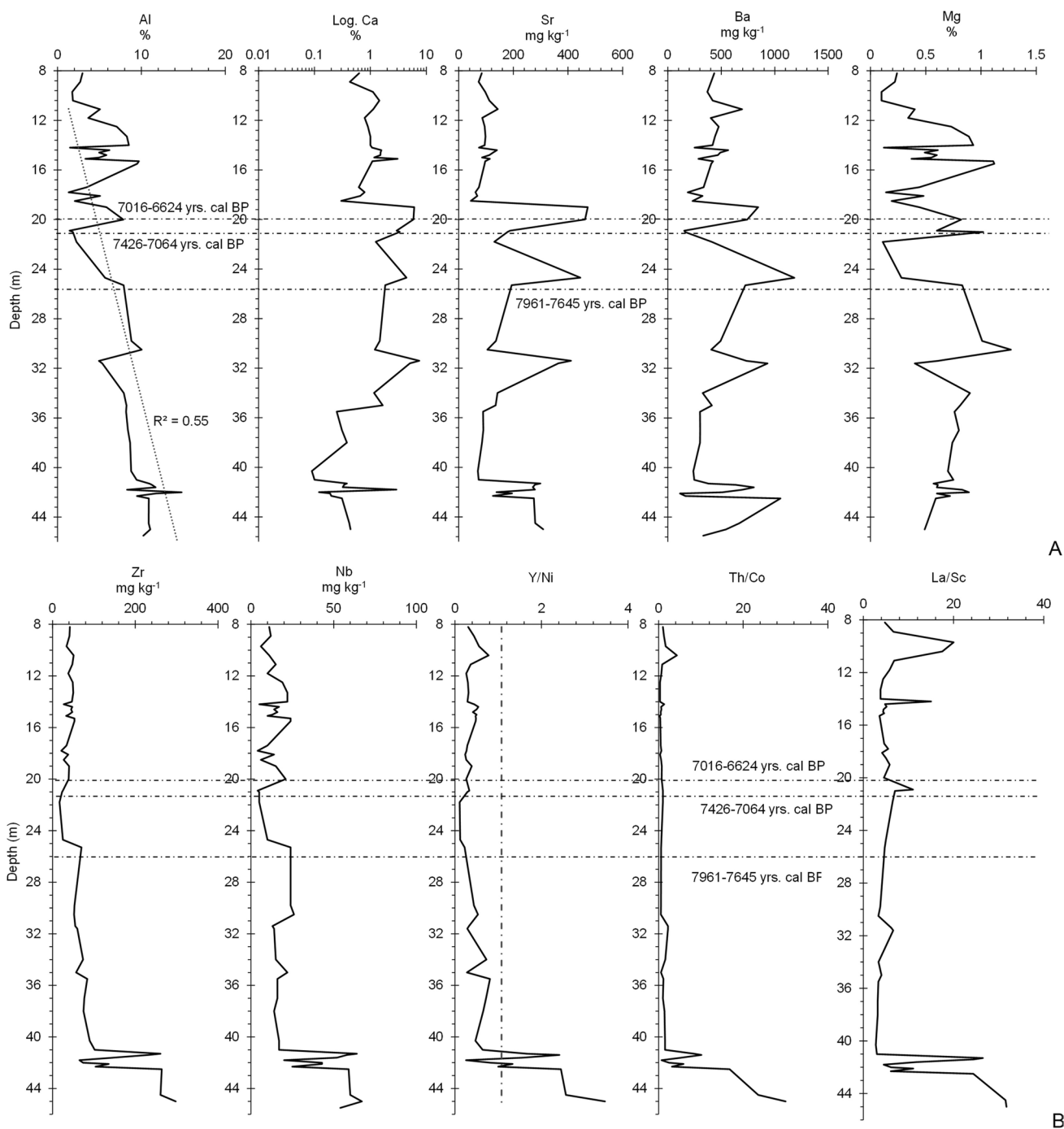
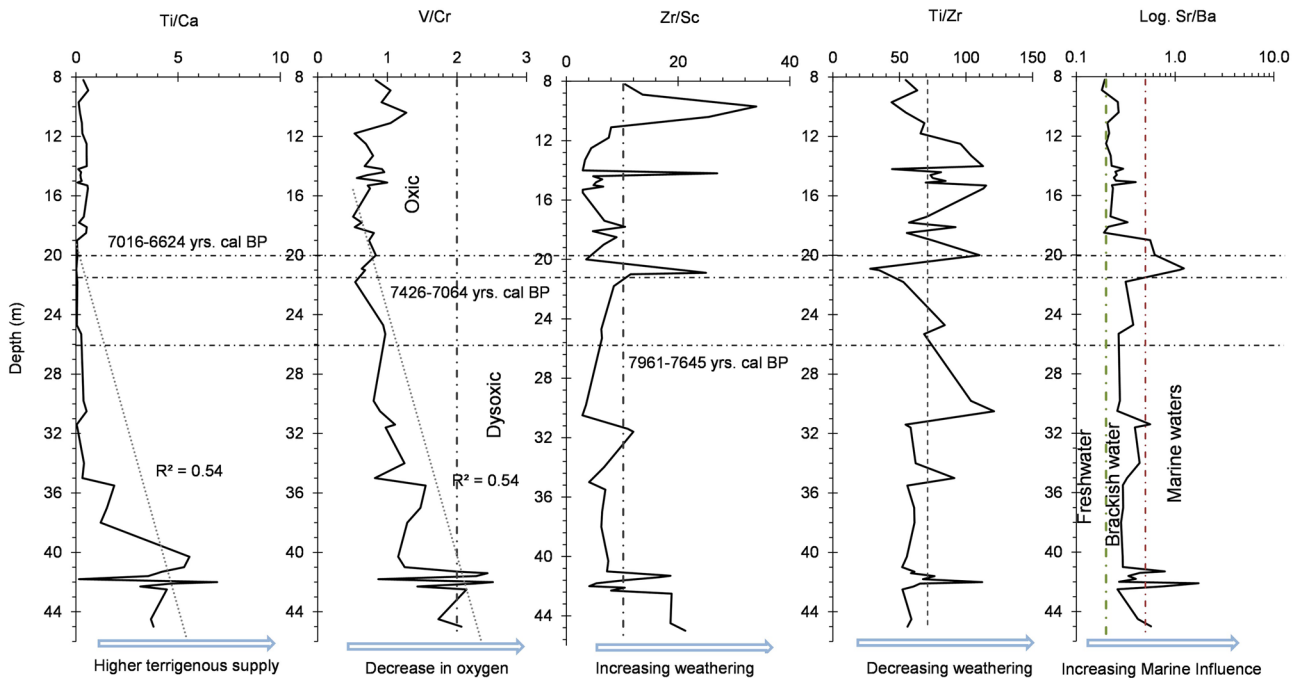


**Fig. 3** Depth plots: **A** Al (%), Ca (%), Sr (mg kg<sup>-1</sup>), Ba (mg kg<sup>-1</sup>), and Mg (%); **B** Zr (mg kg<sup>-1</sup>), Nb (mg kg<sup>-1</sup>), Y/Ni, Th/Co, La/Sc; **C**. Ti/Ca, V/Cr, Zr/Sc, Ti/Zr, and Sr/Ba. The estimated ages have been marked on the graphs. The Ti/Ca and V/Cr graphs show the regres-

sion lines and the respective R<sup>2</sup> values. The scales for the XX axis of Ca and Sr/Ba are logarithmic. **C** contains information on the interpretation of the results

Tupinambá et al., 2007). These rocks justify the predominance of sediments from metamorphic rocks in the core SP10.

The Th/Co versus La/Sc graph is widely used to interpret the source area of clastic rocks (Cullers, 2002). The graph of Th/Co versus La/Sc ratios for core SP10 indicates that it comprises sediments from silica-rich rocks



C

Fig. 3 (continued)

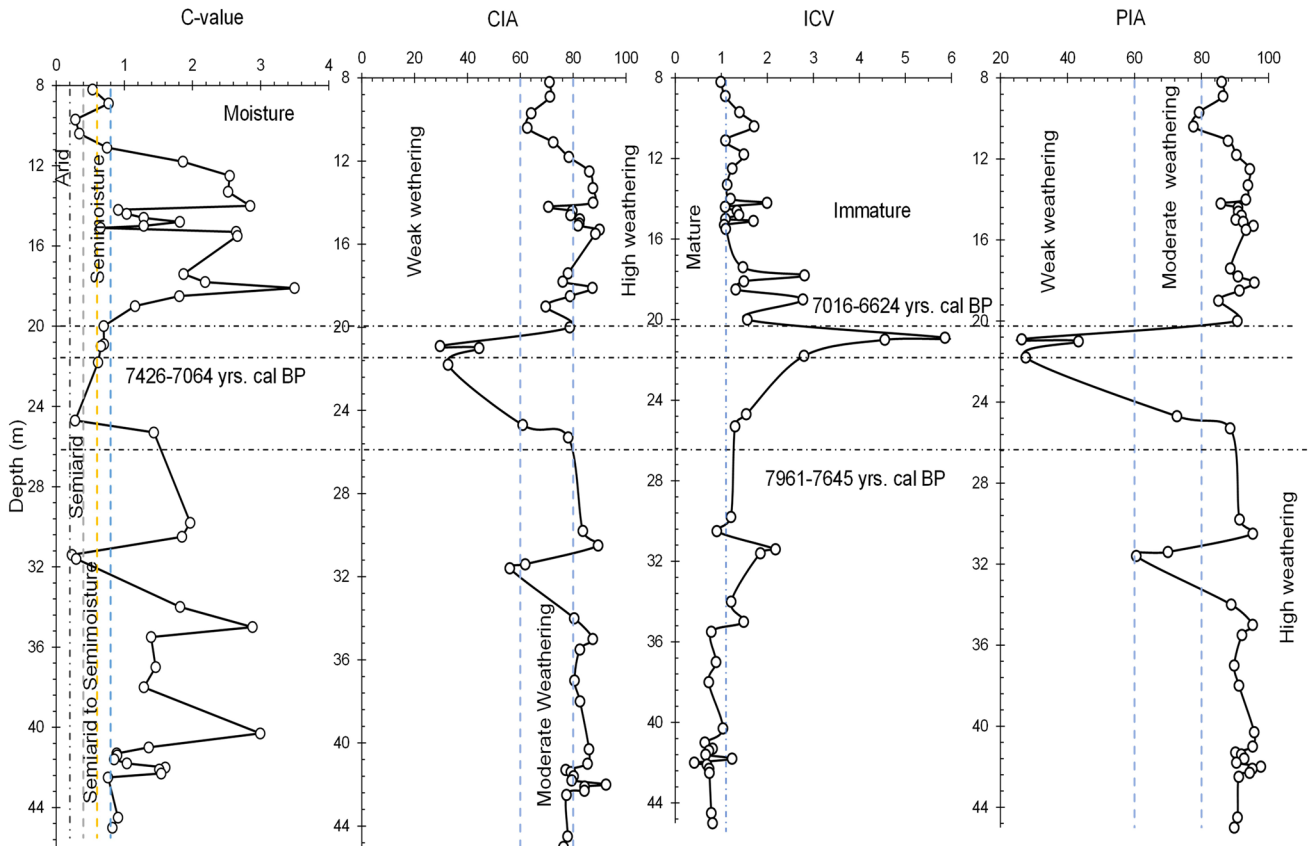


Fig. 4 Graphs as a function of depth of C-Value, CIA, ICV, and PIA indexes. The estimated ages have been marked on the graphs, and information is inferred from these indices

**Table 3**  $\delta^{13}\text{C}$  (‰) and  $\delta^{15}\text{N}$  (‰) values and N total (%) content, between 45.5 and 34.0 m, which is the finest and richer in organic matter section from core SP10

Depth (m)	$\delta^{13}\text{C}$ (‰)	$\delta^{15}\text{N}$ (‰)	N total (%)
34.0	-24.357	10.35	0.0482
35.0	-25.881	ND	ND
35.5	-24.245	10.27	0.1247
37.0	-24.002	8.78	0.1464
38.0	-23.997	8.25	0.1717
40.3	-22.432	8.48	0.1341
41.3	ND	18.42	0.0077
41.4	-26.165	15.86	0.0092
41.6	-26.650	18.29	0.0113
42.0	-27.301	9.85	0.0448
42.3	-23.129	8.21	0.1364
42.5	-26.017	14.51	0.0145
44.5	-24.695	11.17	0.0111
45.5	-24.821	16.33	0.0087
Max	-22.432	18.42	0.1717
Min	-27.301	8.21	0.0077

Legend: *ND* not determined, *Max* maximum, *Min* minimum

(Fig. 7B). These data are corroborated by the region's geology, primarily consisting of gneisses and granites rich in minerals with Si (Heilbron et al., 2020).

The Th/Co versus La/Sc graph (Fig. 7B) indicates that some layers have sediments from silicic rocks. The Pedra Branca Complex, the granitoid body closest to the study area (Fig. 1), formed mainly from the melting of ancient sedimentary rocks (Heilbron et al., 2020; Moterani et al., 2020; Porto Jr. et al., 2018; Valeriano et al., 2011, 2016), could be an essential source of sediment for the region. The Biplot of Th/Co versus La/Sc also suggests the possible contributions from basic rocks. Considering the location of the study area, it can be inferred that it also received contributions from the erosion of the Rio de Janeiro Suite and the Mendanha Alkaline Complex (Fig. 1).

The Pedra Branca Complex, with intrusive basalt dykes, oriented NE–SW, is formed mainly by post-tectonic porphyritic granitoids from the Cambrian, generated from the fusion of ancient sedimentary rocks (Heilbron et al., 2016a, 2016b; Porto Jr. et al., 2018). Similarly, the Rio de Janeiro Suite is relatively close to the core SP10 area and has S-type granitoids (CPRM, 2001). The Mendanha Alkaline Complex (Fig. 1) comprises a group of igneous and metamorphic rocks originating from Cretaceous magmatism (Mota et al., 2012).

The Th, Sc, and Zr/10 triangular graph (Fig. 7D) and the fields defined according to Bhatia and Crook (1986) suggest that the sediments deposited in some levels of the core SP10

resulted from the erosion of rocks formed in the context of an active continental margin and a continental margin with island arcs. The Eastern Terrain of the Ribeira Belt includes two magmatic arc domains that collided with the São Francisco Craton between ca. 900 and 500 Ma (Heilbron et al., 2016b). Furthermore, Heilbron et al., (2000, 2008, 2016b) suggested that the units comprising the western terrain (São Fidelis and Italva Groups) are related to passive margin basins, supporting our hypothesis.

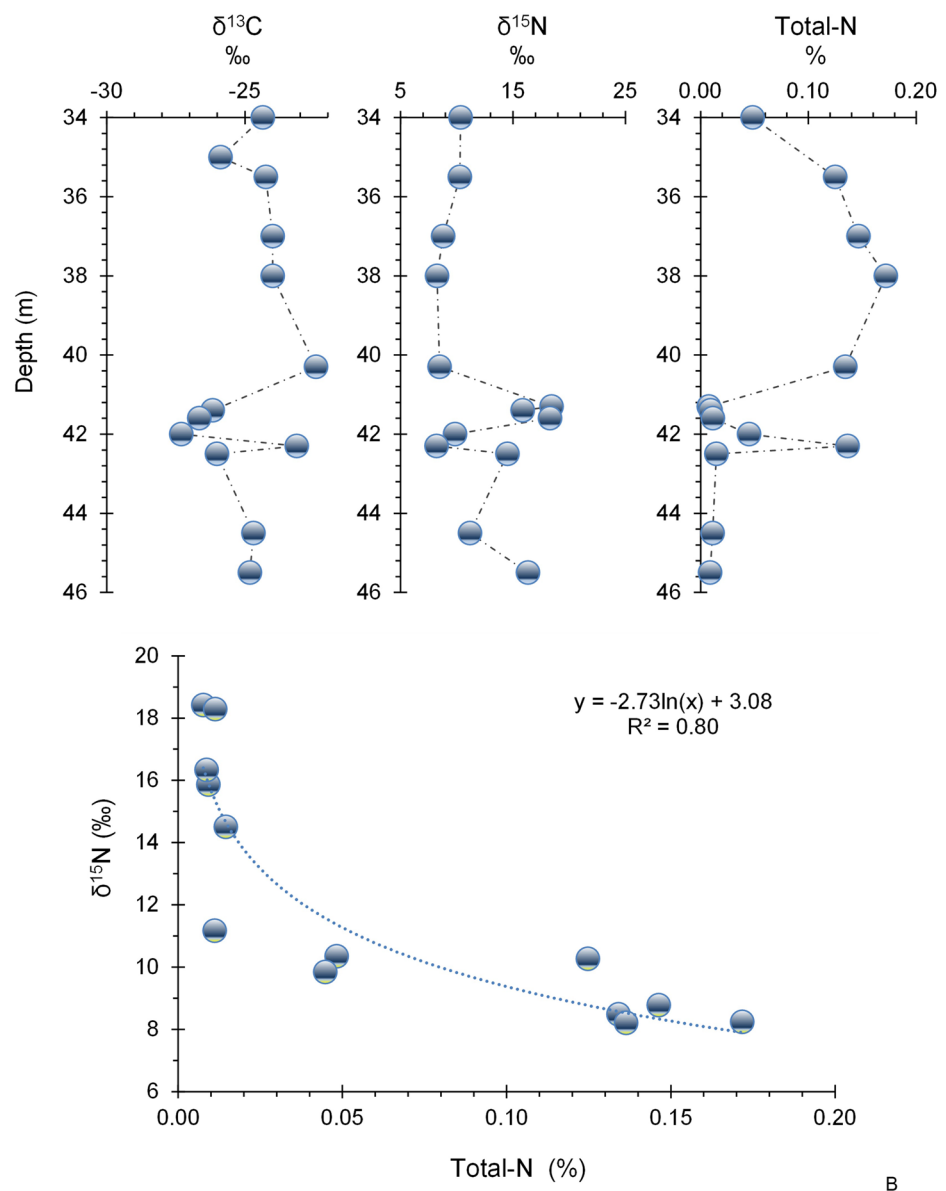
Heilbron et al. (2020) illustrate that the geology of the Rio de Janeiro state is very complex, given the intense tectonic processes of the amalgamation of microcontinents to form the Ribeira Belt. Additionally, several studies indicate that the Rio Negro Complex (Fig. 1) is an arc of volcanic islands with very active magmatism amalgamated with an active margin (Heilbron et al., 2020). Therefore, the signal captured by the ternary diagram (Fig. 7D) and the Cr/V vs. Y/N diagram (Fig. 7A) indicates that the sediments of core SP10 also resulted from the erosion of the metamorphic rocks of the Rio Negro Complex (Fig. 1).

## 5.2 Paleo-weathering

McLennan et al. (1993) utilized the Th/Sc and Zr/Sc ratios in modern deep-sea turbidites to assess the concentration of metals during sediment sorting. In the Zr/Sc ratio, the concentration of Zr is associated with the abundance of the mineral zircon, while Sc represents minerals with a rare earth signature (REE). Zircon is more resistant to weathering processes, resulting in higher Zr/Sc values, indicating a process of sediment recycling; zircon remains in the sediment while other minerals degrade due to weathering (McLennan et al., 1993). Conversely, the Th/Sc ratio is related to igneous chemical differentiation processes, with Th being more abundant in felsic rocks and Sc in mafic rocks (McLennan et al., 1993).

The relations between Th/Sc versus Zr/Sc were used (as described by McLennan et al., 1993) to detect changes in sediment composition and alterations in weathering processes along the core SP10 (Fig. 8A). The Th/Sc versus Zr/Sc diagram (Fig. 8A) reveals that specific sediment layers have higher mafic sources and have been affected by low to intermediate degrees of weathering. On the other hand, there are layers in core SP10 with higher proportions of sediments from felsic sources because they have been exposed to intense weathering or were sourced by rocks enriched in silica minerals. From the relatively high La/Sc and Zr/Sc values (Fig. 3B, C) and Th/Sc (Figure Supplementary 1 or Fig. S1), it can be inferred that the sediments sourced by felsic rocks resulted mainly from the intense weathering of granitic rocks. At the core base, between 45 and 36 m, fine (Fig. 2A), poorly sorted sediments (Appendix 1), rich in elements such as Th, La, Y (Fig. S1), Zr, and Nb (Fig. 3B)

**Fig. 5** **A** Depth plot of  $\delta^{13}\text{C}$  (‰),  $\delta^{15}\text{N}$  (‰), and Total-N (%) values in the section between 45.5 and 34 m, which is the finest and richer in organic matter. **B** Biplot of  $\delta^{15}\text{N}$  (‰) versus Total-N (%); the regression line and respective  $R^2$  and the line equation are also shown



should be related to a proximal depositional environment with a significant continental contribution.

Titanium (Fig. S1) and Zircon (Fig. 3B) concentrations increased at the base of the core SP10 (45–41 m) in fine sediments rich in OM (Fig. 2A, B). These elements are associated with different minerals (Koinig et al., 2003; Taboada et al., 2006). Titanium minerals can degrade more quickly than Zircon (Fitzpatrick & Chittleborough, 2002). Titanium can dissolve in water (Kryc et al., 2003; Skrabal, 1995) but may be retained in organic matter-rich sediments. Conversely, zirconium tends to increase in more weathered sediments because zircon is a mineral that is more resistant to weathering (McLennan et al., 1993). Cyclical increases in the Ti/Zr ratio were recorded, indicating phases in which the sediments were less reworked (Fig. 3C).

Based on the Biplot of ICV versus CIA (Fig. 8B) and the depth plots of CIA and PIA (Fig. 4), the core SP10 is characterized by the predominance of moderately to intensely weathered sediments due to leaching of minerals linked to Na, K, and Ca from the matrix rock. The depth plot of the ICV values (Fig. 4) indicates the prevalence of mature sediments at the base of the core SP10 and cyclical occurrences of more immature sediments. For instance, low-weathered and immature sediments were identified in the interval 21.8–20.9 m (Figs. 4, 8B).

### 5.3 Depositional environment

Salinity conditions in the study area were accessed through the Sr/Ba ratio. The Sr/Ba ratio serves as an empirical

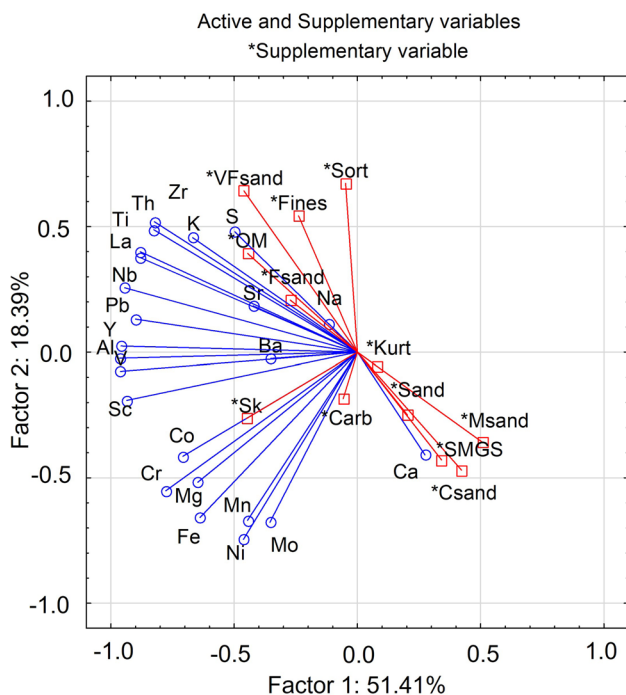


**Fig. 6** PCA Factor 1 versus Factor 2 based on the geochemical and textural results. Abbreviations: *SMGS* sediment mean grain size, *Sort* sorting, *Sk* skewness, *Sand* sand fraction, *Fines* fine fraction, *Csand* coarse sand fraction, *Msand* medium sand fraction, *Fsand* fine sand fraction, *VFsand* very fine sand fraction, *OM* organic matter, *Carb* carbonates Kurt kurtosis

indicator of paleosalinity (Liu, 1980), with Sr directly deposited from seawater, while barium is readily adsorbed by clay minerals and fine clastic sediments (Liu et al., 1984; Wang, 1996; Xu et al., 2011). Wang et al. (2021) also suggest that Ba is easily adsorbed by clay minerals, colloids, and organic matter due to its large ionic radius and lower hydration energy, while Sr is a more mobile element that is not easily adsorbed by organic matter and clay fraction during transport. Therefore, sediments of terrestrial origin tend to have higher concentrations of Ba. Thus, Wei and Algeo (2020) suggest that Sr/Ba values of  $< 0.2$  are observed in freshwater, between 0.2 and 0.5 are typical of brackish waters, and  $> 0.5$  are found in marine waters. Throughout core SP10, Sr/Ba ratios varied between 0.2 and 0.5 (Fig. 3C), indicating that the site was mainly a brackish environment, except at its base (between 42.1 and 41.3 m) and middle section (mainly between 21.8 and 19 m) where Sr/Ba ratios are  $> 0.5$  indicating the presence of marine waters.

Despite this, there is a generally more significant marine influence in the middle portion of the core (interval  $\sim 35$ –18.5 m), where there is a significant increase in Ca, Sr, and Mg (Fig. 3A) and carbonate (Fig. 2B) values.

The increase in Ca, Sr, and Mg can be justified since these elements are related to sediments of marine origin due to their assimilation into the carbonate shells and skeletons of marine organisms (Kim et al., 1999). This interval of higher marine water influence agrees with the observations of Castelo et al. (2021) that suggested that around 7.8 ka BP, the marine transgression flooded Marambia Cove.

The median diameter versus skewness graph (Fig. 9) and the fields proposed by Noori et al. (2016) indicate that the sediments from the section between 44.5 and 34 m were deposited in general under "calm water" conditions. The relatively high organic matter S, V, and Pb contents (Fig. 2B) and the values of  $V/Cr > 2$  (Fig. 3C; Jones & Manning, 1994; Powell et al., 2003) indicate low oxic conditions between 42 and 36 m, due to higher confinement.

Following this calmer phase, there is an upward increase in grain size, indicating a progressive intensification of hydrodynamics towards the core's top (Fig. 2A). The graph of Fig. 9 also suggests that the layer at 42.1 m and the interval 33–19 m, characterized by increased coarse and medium sand fractions (Fig. 2A), were deposited in a wave-influenced environment.

The intensification of hydrodynamics in the upper section of the core SP10 (between 41 and 8.2 m) determined the reduction in organic matter (Fig. 2B) and Al (Fig. 3A) contents and favored the oxygenation of the sediments (according to the  $V/Cr$  values  $< 2$ ; Fig. 3C). Organic matter and Al contents tend to increase in fine-grained sediment (e.g., Ho et al., 2010; Silva et al., 2022). Thus, we can deduce that most of the sediments of core SP10 were deposited in oxidizing conditions except its lower section, between 45 and 41 m.

The relatively more positive skewness values (Appendix 1), corresponding to fine and medium sands (found mainly between 34 and 8.2 m), suggest a weak tendency for sediments to be reworked, transported, and deposited close to the bottom. Thus, changes in hydrodynamics and the characteristics of the transport agent may have influenced not only the sediment grain size but also its geochemical characteristics (related to its mineralogical composition and redox state).

General changes in detrital supply, especially those supplied by fluvial processes (Govin et al., 2012), were analyzed with the Ti/Ca ratio. The values of this ratio are higher at the base of the core between 45 and 35 m (where the sediments are finer) and lower in the upper section between 34 and 8 m (Fig. 3C). It suggests a decrease in the supply of fine-grained terrigenous sediments and a deposition of higher amounts of biogenic particles (e.g., mollusk shells), as indicated by the relatively high carbonate (Fig. 2B) and Ca contents (Fig. 3A).

However, according to Deng and Qian (1993) and Fu et al. (2015), high Sr/Ba values can be associated with high salinity and warm and arid environments. The C-value allowed to

**Fig. 7** **A** Cr/V vs. Y/Ni diagram (Hiscott, 1984), suggesting ultramafic (UM), metamorphic (ME) and granitic (GR) rock fields; **B** Th/Co versus La/Sc diagram showing the composition of the source rock (and inferred fields based on Cullers, 2002). **C** Th-Sc-Zr/10 discrimination plot for inference of tectonic settings, based on Bhatia and Crook (1986)

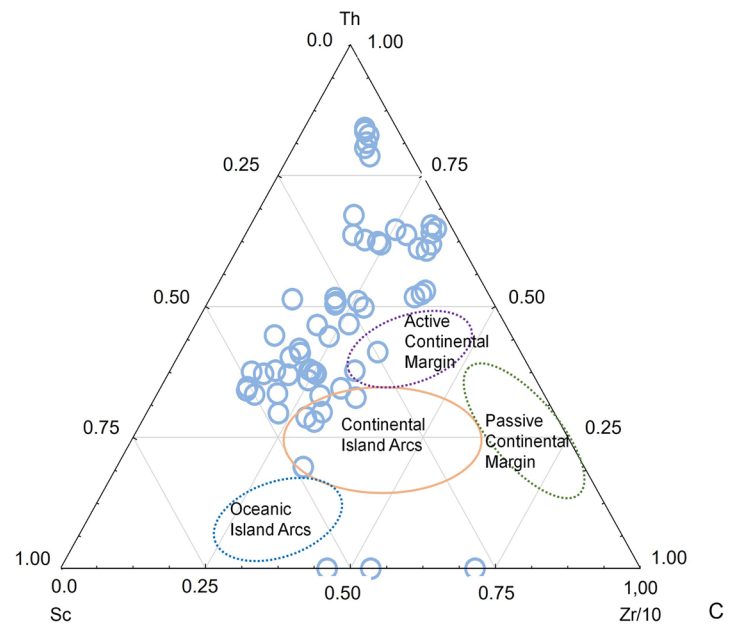
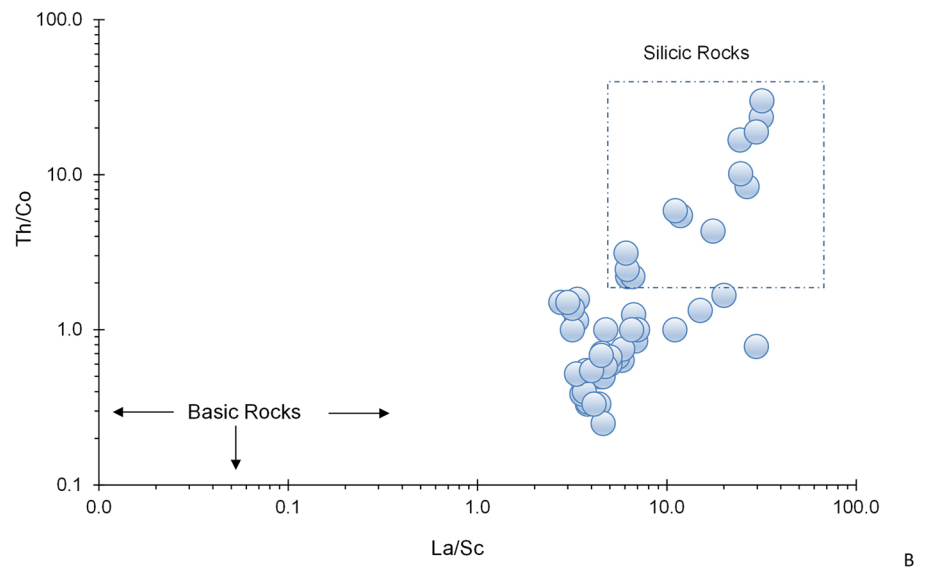
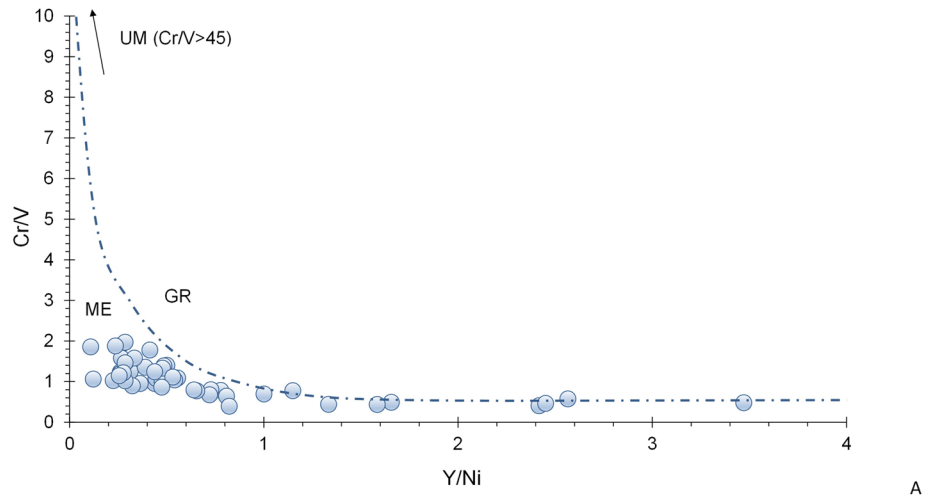
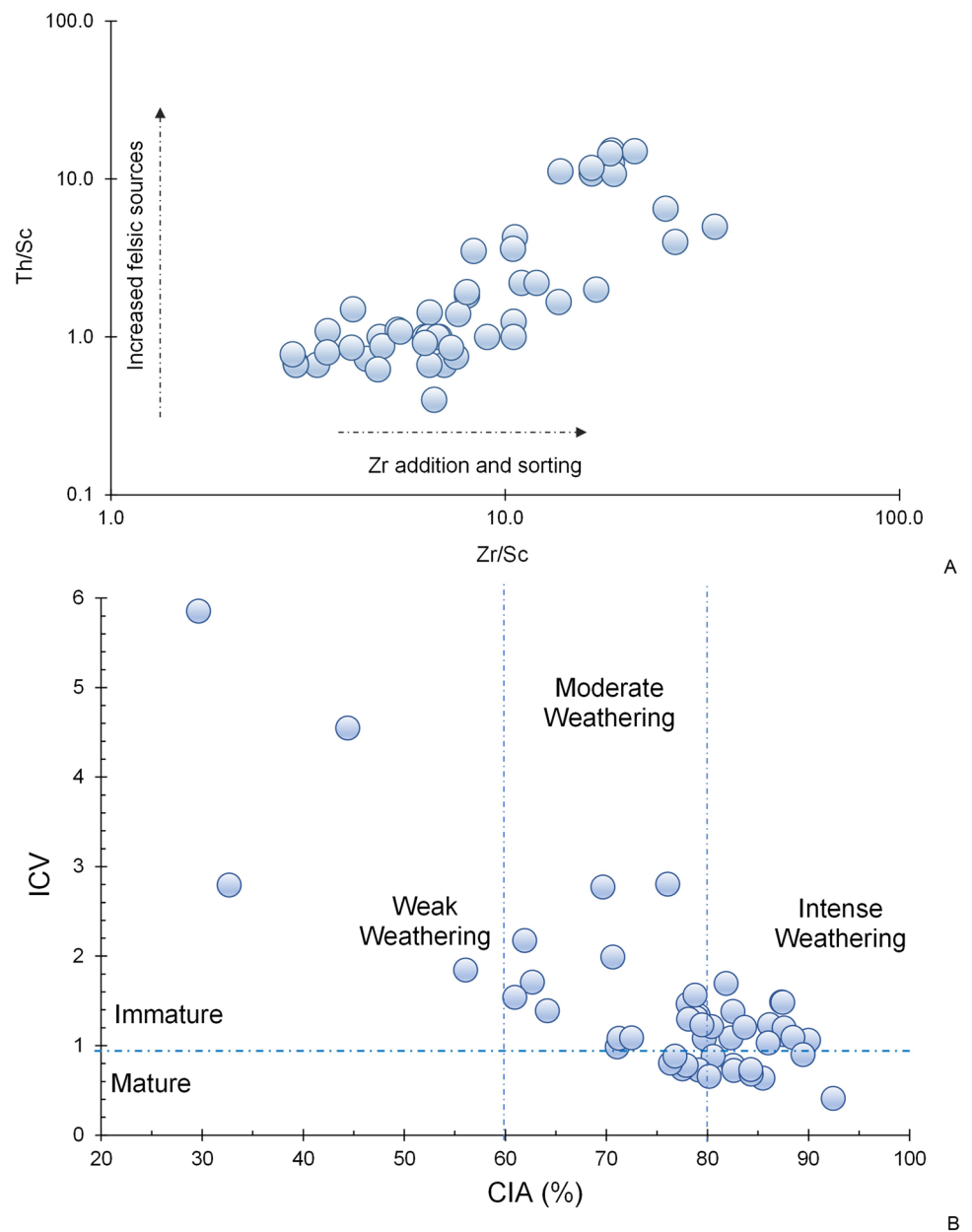


**Fig. 8** **A** Relationship between Th/Sc versus Zr/Sc, indicating increased felsic sources and increased sediment weathering (based on McLennan et al., 1993). **B** Biplot of ICV versus CIA, showing the degree of sediment weathering (based on Cox et al., 1995; Nesbitt & Young, 1984)



access temporal changes in humidity (Fig. 4). According to this index, there were several periods of drought during the Holocene (Fig. 4). The driest (semiarid) periods were identified around 42–41 m, 31 m (Fig. 4A) and between 24 and 20 m (Fig. 4A). All these events were followed with shifts in the Sr/Ba values (Fig. 3C) agreeing with the statements of Deng and Qian (1993) and Fu et al. (2015).

The C-value depth plot also indicates that most core layers were deposited under humid climatic conditions (Fig. 4). Higher rainfall phases were identified between 42 and 33 m, 31 and 25 m, 19 and 15 m, and 14 and 11 m (Fig. 4).

#### 5.4 Source of organic matter for the sediment

We can deduce that in core SP10, the interval between 40.3 m and 34.0 m, with  $\delta^{13}\text{C}$  values varying between  $-27.30\text{‰}$  and  $-22.43\text{‰}$  and  $\delta^{15}\text{N}$  between  $8.21\text{‰}$  and  $18.42\text{‰}$ , likely received organic matter mainly from a mangrove environment with additional marine sources (Fig. 10). Several studies support these inferences.

Terrestrial organic matter exhibits lower  $\delta^{13}\text{C}$  and  $\delta^{15}\text{N}$  values than marine organic matter (Li et al., 2016; Sampaio et al., 2010; Vizzini et al., 2005). The  $\delta^{13}\text{C}$  values vary in C3 terrestrial plants from  $-33\text{‰}$  to  $-24\text{‰}$ , C4 terrestrial plants from  $-16\text{‰}$  to  $-10\text{‰}$ , and soil organic matter from  $-32\text{‰}$  to  $-20\text{‰}$  (Kendall et al., 2001; Meyers,

**Fig. 9** Sediment deposition environments were estimated from the skewness versus the sediments' median diameter diagram and the fields following Noori et al. (2016). The main intervals in which the fields marked on the graph are recorded are in brackets

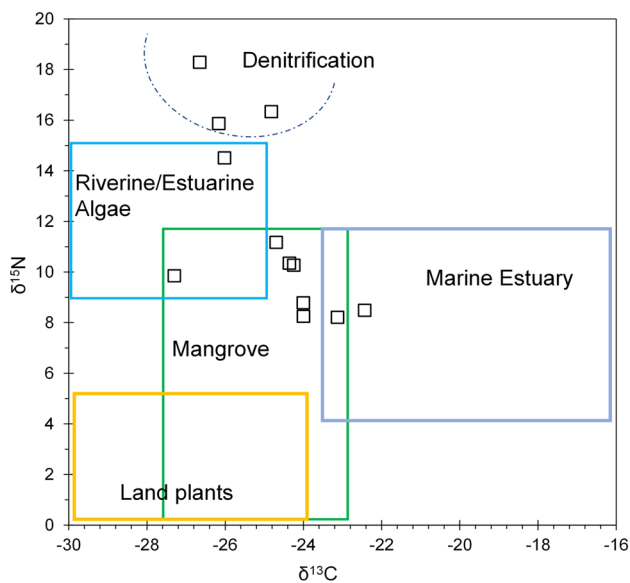
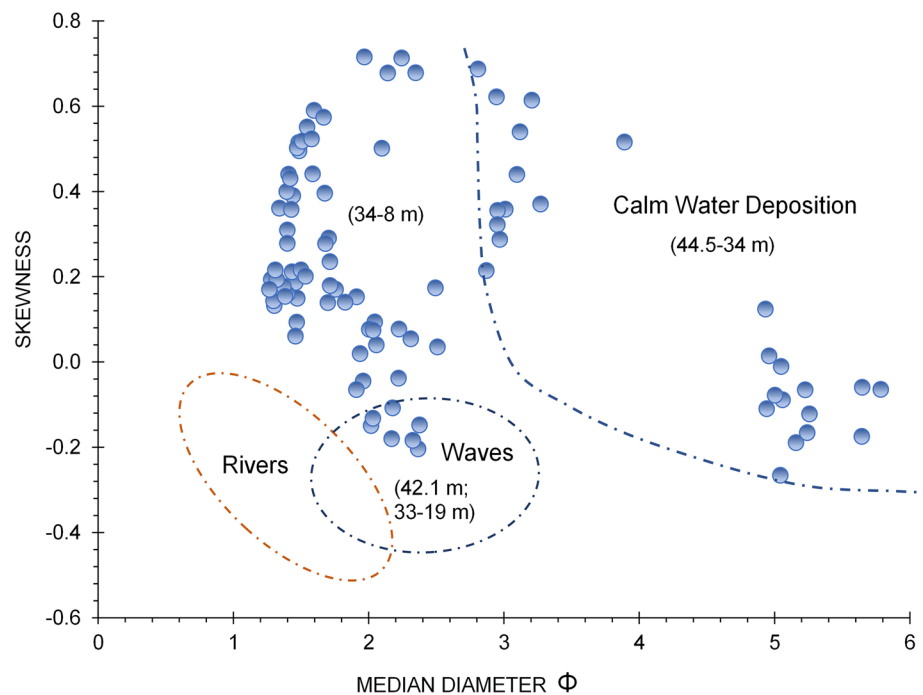


**Fig. 10** Organic matter sources in the lower section of core SP10 accessed from  $\delta^{13}\text{C}$  versus  $\delta^{15}\text{N}$ . The suggested fields are based on several authors (e.g., Carneiro et al., 2021; Deines, 1980; Kendall et al., 2001; Martins et al., 2016; Meyers, 2003; Ye et al., 2017)

2003). According to Meyers and Ishiwatari (1993), values of  $\delta^{13}\text{C} > -20\text{‰}$  can indicate planktonic algae in lacustrine and marine environments. Ye et al. (2017) observed  $\delta^{13}\text{C}$  values from freshwater plankton between  $-28.4\text{‰}$  and  $-32.6\text{‰}$  and enriched  $\delta^{15}\text{N}$  ( $> 6.7\text{‰}$ ). Similar values were observed in other rivers/estuaries, such as the Mississippi

River estuary (Wang et al., 2004) and the San Pedro River (Brooks et al., 2007). Deines (1980) found  $\delta^{13}\text{C}$  values in a bay-type region ranging between  $-18\text{‰}$  and  $-22\text{‰}$ . Martins et al. (2016) observed in the transition region of Guanabara Bay typical  $\delta^{13}\text{C}$  planktonic signatures varying between  $-25.3\text{‰}$  and  $-16.2\text{‰}$  and  $\delta^{15}\text{N}$  oscillating from  $4.6\text{‰}$  to  $11.2\text{‰}$ .

Smith and Epstein (1971), Bouillon et al. (2008), and Wang et al. (2014) reported  $\delta^{13}\text{C}$  values in the  $-35\text{‰}$  to  $-20\text{‰}$  range for mangroves. Similar  $\delta^{13}\text{C}$  values were observed in South Florida in *Rhizophora mangle*, a species typical of mangrove environments (Lin & Sternberg, 1992). Rodelli et al. (1984) found in Malaysian ecosystems the following  $\delta^{13}\text{C}$  values for mangroves  $\sim -27\text{‰}$ , for marine phytoplankton from  $-22\text{‰}$  to  $-20\text{‰}$  and a variety of other algae from  $-22.5\text{‰}$  to  $-14.8\text{‰}$ .

Sweeney and Kaplan (1980) observed in sediments of marine origin  $\delta^{15}\text{N}$  values of  $+10\text{‰}$ . In a mangrove, nitrogen sources enriched in  $\delta^{15}\text{N}$ , such as nitrogen-rich products by anaerobic bacteria or nutrient-rich estuarine water, may be found (Heaton, 1986).

The higher  $\delta^{15}\text{N}$  values recorded at the base of core SP10 may have resulted from isotopic fractionation during denitrification. Denitrification transforms nitrates and other substances into nitrogen gas ( $\text{N}_2$ ) by denitrifying bacteria. In sediments without atmospheric oxygen, denitrifying prokaryotes can use nitrate to oxidize organic compounds (anaerobic respiration) (Chen & Strous, 2013; Shapleigh, 2013). Through this process, some of the nitrate in the soil is returned to the atmosphere in the form of nitrogen gas.



The return of the light isotope of nitrogen to the atmosphere results in a higher value of  $\delta^{15}\text{N}$  (Heaton, 1986). Thus, higher  $\delta^{15}\text{N}$  values should be related to anoxic conditions in the base of core SP10, where more active denitrification processes and a more significant loss of the nitrogen light isotope to the atmosphere may have occurred. The negative correlations between  $\delta^{15}\text{N}$  and total-N values corroborate these inferences, indicating a severe impact of organic matter degradation in nitrogen isotope values (Fig. 5B).

The layers of the base of core SP10 also show more negative  $\delta^{13}\text{C}$  values (Fig. 5A), probably due to organic matter diagenetic changes. Several authors also observed this relationship (e.g., Freudenthal et al., 2001; McArthur et al., 1992; Nakatsuka et al., 1995; Prahl et al., 1997).

### 5.5 Evolution of the sedimentary environment

The cyclical occurrence of wetter phases alternating with drier ones, indicated by the C-value (Fig. 4), agrees with the observations of Suguio et al. (1989). These authors observed erosional phases in fluvial deposits and changes in the vegetation cover in different areas from SE Brazil, such as between 10.0 and 8.5 ka BP, 7.0 and 6.0 ka BP, and 5.0 and 4.0 ka BP, due to increased precipitation. The early Holocene moister phase (between 10.0 and 8.5 ka BP) was also recorded at Salitre, central Brazil (Ledru, 1993). Coarse sediment fans were deposited in Lago do Pires, SE Brazil, between 9.0 and 8.0 ka BP during this moister phase (Behling, 1995; Servant et al., 1989).

The study region may have experienced periods of severe drought followed by heavy rainfall phases, resulting in the mobilization of sediments. According to the CIA, PIA, and ICV values presented in Fig. 4, highly weathered and mature sediments were accumulated during the wetter phases; on the contrary, during the drier phases, more immature and less weathered sediments were deposited (Fig. 4).

In the core base, between 45 and 41 m, the relatively high values of Ti/Ca, Zr, and Nb suggest a predominant supply of sediments from continental rocks, and Th/Co, La/Sc, and Y/Ni indicate the presence of sediments primarily sourced from proximal felsic rocks. The probable source of these sediments is the Pedra Branca Complex, close to the study area, composed chiefly of granitoids with a high concentration of felsic minerals, such as plagioclase and quartz (Porto Jr. et al., 2018). The sources of organic matter suggest that the environment was a mangrove visited by calm tidal currents, favorable to the accumulation of organic matter. The highly weathered sediments in this section (see CIA and PIA values; Fig. 4) suggest their high chemical and physical alteration under a wetter period (indicated by C-value > 0.8; Fig. 4). The tidal currents continuously reworked the sediments, but the presence of poorly sorted

sediments is probably related to mass displacements through sloping areas during the rainiest periods.

The interval between 45 and 41 m was probably related to the humid period recorded in SE Brazil by Suguio et al. (1989) between 10.0 and 8.5 ka BP. The study area was probably a protected tidal plain estuary with mangroves at that time. The sea level was lower than the current one but was rising (Angulo et al., 2006; Lambeck et al., 2014).

Studies conducted over the last 10 years in the Sepetiba Bay region (e.g., Dadalto et al., 2022; Reis et al., 2020) and adjacent continental shelf (Friederichs et al., 2013) have revealed the complexity of the region evolution, particularly over the last 22 ka, when global climate changes led to the melting of glaciers found in temperate latitudes and the consequent sea level rise. River basins extended over a large part of the continental shelf during glaciation (Reis et al., 2020). During the marine transgression, in addition to the filling of the river channels (excavated during the regression), there are indications of the formation of sandy barriers segmented by tidal channels (Reis et al., 2020). The old tidal channels migrated laterally and were filled in as the sea level rose. Sandy barriers were formed and destroyed along the transgression (Reis et al., 2020), exposing or protecting segments of the coastal plain. The position, extent, and configuration of the barrier islands, among other factors, may also have influenced the granulometry and compositional characteristics of the sediment and the oceanic influence in the study area (documented, for example, by the Sr/Ba values, Fig. 3C).

However, it should be noted that the rapid rise in sea level significantly increased the marine influence and hydrodynamics in the study area. That is indicated in the interval 35–8 m by the low Ti/Ca values (Fig. 3C), increased Ca contents (related to mollusk shells; Fig. 3A), and the substantial rise in the sand fraction (Fig. 2A). The values of the Y/Ni, Th/Co, and La/Sc ratios (Fig. 3B) sharply decline from 41 m onwards, suggesting a significant shift in the sediment composition. From 41 m onwards, the sediments started exhibiting a more mafic mineralogical composition. These characteristics remained identical until 14.2 m. Between 11.1 and 8.9 m, there is again a more significant felsic component in the sediment composition (as indicated by the La/Sc values; Fig. 3B).

It can be inferred that the mafic sediments supplied to the study area, from 41 m onwards, originated in the Rio Negro Complex, located to the north of Sepetiba Bay (Fig. 1). This complex comprises orthogneisses, rich in mafic minerals such as biotite and poikiloblastic hornblende, along with a smaller proportion of other felsic minerals, such as plagioclase and quartz (Tupinambá et al., 2012). This change in the source area of the sediments is probably associated with the rise in sea level and the role of coastal drift in the distribution of materials (enriched in mafic components) supplied

by the rivers that flow into Sepetiba Bay. These data suggest that the intercommunication between Sepetiba Bay and the study area was possible and easy.

Changes in rainfall intensity may also have influenced the characteristics of the sediments deposited in the study area. The drought period recorded in core SP10 from  $\sim 7.5$  to 7.0 ka cal BP (between 25 and 21 m) was one of the driest events of the Holocene in south-central Brazil (Salgado-Labouriau et al., 1998). Notably, a decrease in CIA and PIA values was recorded during this period (Fig. 4), indicating that the deposited sediments were less weathered during this dryness phase. The sudden increase in ICV values (Fig. 4) marks the presence of immature sediments. Ti/Ca ratios were low in this arid phase, and Ti/Zr sharply decreased (Fig. 3C), probably due to the restricted supply of detrital sediments to the study area. However, a notable rise in the Sr/Ba ratio was recorded (Fig. 3C), which indicates that this dry period was combined with a more significant marine influence in the area.

Paleoclimate records in the regions influenced by the South American Low-Level Jet (SALLJ) (Zhou & Lau, 1998), which transports moisture from the Amazon basin core to the southwest of Brazil during the southern summer, indicate a consistent long-term trend of increasing precipitation starting around the mid-Holocene ( $\sim 7.0$ – $6.0$  ka BP). This trend is supported, for instance, by records from Botuverá Cave (southern Brazil) (Cruz et al., 2005), Lake Titicaca (the Altiplano, Peru; Baker et al., 2001), Laguna La Gaiba (the central lowlands, Bolivia; Whitney & Mayle, 2012), which are influenced by the SALLJ. This progressive increase in rainfall may be linked to the strengthening of the monsoon, following a precession cycle, as orbital forces increase the insolation of the southern summer (Berger & Loutre, 1991). This event is recorded in core SP10 between 19 and 15 m (according to the C-values; Fig. 4). This core also records another wetter phase between 14 and 11 m (according to the C-values; Fig. 4). These rainier phases should be contemporaneous of the wet times noticed by Suguio et al. (1989) between 7.0 and 6.0 ka BP, and 5.0 and 4.0 ka BP. During these humid phases, Ti/Zr peaks are observed (Fig. 3C), indicating the supply of less weathered sediments introduced by the rivers into the oceanic system and transported to the study area by the littoral drift.

The slight increase in La/Sc values in the interval  $\approx 11.1$ – $9$  m (Fig. 3B) indicates that the sediment progressively included an increasing proportion of felsic particles. During this phase, the climate became drier again, and the mean grain size decreased, but the sedimentary environment remained oxygenated; salinity decreased, indicating less oceanic influence in the study area. The more negative skewness values also indicate a greater fine sediment accumulation tendency. The sediment has become better sorted, consisting of one primary mode, which indicates

a preponderance of aeolian transport. Proximal sediments were deposited during this phase, probably from the Pedra Branca Complex (Fig. 1). The study area was now part of a sandy coastal plain.

During this phase (after  $\approx 4.0$  ka BP), the connection of the study area with Sepetiba Bay was more restricted. The extension and strengthening of Marambaia Barrier Island (Friederichs et al., 2013) may have barred the direct connection between the waters of Sepetiba Bay and the study area, hindering the arrival of sediment from the erosion of the Rio Negro Complex (Fig. 1).

## 6 Conclusion

Core SP10 has preserved significant variations in depositional conditions during the Holocene. The Sr/Ba ratio suggests that the study area predominantly experienced the influence of brackish waters, interspersed with periods of higher marine influence.

The C-value indicates that the study region may have experienced periods of severe drought followed by heavy rainfall phases. During heavy rainfall, the sediments underwent intense to moderate chemical weathering (as indicated by geochemical indices CIA, PIA, ICV).

The core base, between 45 and 41 m, would correspond to the wet period in SE Brazil between  $\approx 10.0$  and 8.5 ka BP. During this period, calmer hydrodynamic conditions prevailed, allowing the deposition of fine sediments enriched in organic matter provided mainly by mangrove sources (as indicated by the  $\delta^{13}\text{C}$  and  $\delta^{15}\text{N}$  of organic matter). The degradation of organic matter led to dysoxic conditions (indicated by the V/Cr ratio). In the context of lower sea levels, the study area was confined and received sediment from nearby areas, probably mainly from the Pedra Branca Complex. This period was interrupted by a dry phase.

In the 41–12 m interval, the study area began to receive a significant sediment contribution from the Rio Negro Complex, located to the north of Sepetiba Bay. The hydrodynamics strengthened, and the sedimentary environment transitioned to oxic conditions (as indicated by the V/Cr ratios). Due to the rise in sea level, the coastal drift brought sediment supplied by the rivers that flowed into Sepetiba Bay for the study area.

From  $\sim 7.5$  to 7.0 ka cal BP (between 25 and 21 m), there was a period of drought (according to the C-value). The Ti/Zr decreased dramatically, probably due to a decrease in the supply of detrital sediments. The CIA and PIA values indicate a significant reduction in the chemical weathering (immaturity) of the sediments deposited during this period. The Sr/Ba ratio values suggest a more significant marine influence in the study area.

In the section between 21 and 8 m, there are two significant increases in the C-value (between 19–16 m and 14–11 m), which may be related to the wet phases recorded in SE Brazil, between  $\approx 7.0$ – $6.0$  ka BP, and  $\approx 5.0$ – $4.0$  ka BP. During these wet phases, high-weathered sediments, with a significant component from the Rio Negro Complex, were accumulated. The rivers that flowed into Sepetiba Bay probably introduced this mafic component, which was transported to the study area by littoral drift. At this time, the direct connection between the waters of Sepetiba Bay and the study area would be easy.

However, in the 11–9 cm interval of core SP10, the deposition of felsic sediments increased, indicating greater confinement and less connection with Sepetiba Bay, probably due to the development of the Marambaia Barrier Island.

The results from core SP10 illustrate the combined effect of the geology, sea level rise during the Holocene transgression, climatic and coastal geomorphological changes, and alterations in fluvial, wave, and tidal influence on sediment transport in the study area. The results document the influence that the development of barrier islands, namely Marambaia Barrier Island, can have on the characteristics of the sediments that accumulate in the coastal region.

**Supplementary Information** The online version contains supplementary material available at <https://doi.org/10.1007/s43217-024-00170-0>.

**Acknowledgements** The authors would like to thank the Editor and the anonymous reviewers for their contributions which have helped to improve the work. This paper is a contribution of the projects of Conselho Nacional de Desenvolvimento Científico e Tecnológico of Brazil, CnPQ (project process # 443662/2018-5) and the Fundação de Amparo à Pesquisa do Estado do Rio de Janeiro—FAPERJ (Edital “PENSA RIO”, process # E-26/010.003024/2014 and Edital Projetos Temáticos no Estado do Rio de Janeiro—2021, process # E-26/211.278/2021) and the project “Apoio a Entidades Estaduais 2014” (process E-26/010.002642/2014). Fabrício Damasceno, thanks for the PhD fellowship to FAPERJ (process #E-26/204.093/2022) and to Coordenação de Aperfeiçoamento de Pessoal de Nível Superior – Brasil (CAPES) – Finance Code 001, with master’s scholarship to FLD. Murilo is grateful for the PhD fellowship to the National Council for Scientific and Technological Development, CNPq (Process 141863/2023-4). Virginia Martins would like to thank the CNPq (process #302676/2019-8) and FAPERJ (process # E-26/202.927/2019 and process # E-26/200.333/2023) for the research grants. Antonio Tadeu dos Reis also thanks CNPq and FAPERJ for the research grants (process #309779/2021-9 and process #200.427/2023, respectively).

**Author contributions** F.L.D.: Data acquisition, formal data analysis, mapping, writing—original draft; M.V.A.M.: Data acquisition, data curation, formal data analysis, investigation, supervision, writing and editing the original draft, financial acquisition; J.V.G.: Data curation, investigation, supervision; A.T.R.: Conceptualization, methodology, data acquisition, financial acquisition; M.B.S.: Formal data analysis, writing—original draft; L.C.S.: Formal data analysis, writing—original draft; A.P.S.: Formal data analysis, writing—original draft; V.F.: Formal data analysis, writing—original draft; K.F.C.: Editing the original draft; M.A.M.: Writing—Original Draft; R.C.L.F.: Data acquisition, Investigation; M.G.: Investigation.

**Funding** Open access funding provided by FCTIFCCN (b-on). Financing received from: Conselho Nacional de Desenvolvimento Científico e Tecnológico of Brazil, CnPQ—processes # 443662/2018-5, # 302676/2019-8, # 141863/2023-4 and #309779/2021-9. Fundação de Amparo à Pesquisa do Estado do Rio de Janeiro—FAPERJ (Edital “PENSA RIO”, process # E-26/010.003024/2014; Edital Projetos Temáticos no Estado do Rio de Janeiro—2021, process # E-26/211.278/2021 and the project “Apoio a Entidades Estaduais 2014” (process E-26/010.002642/2014) and research grants: processes #E-26/204.093/2022, # E-26/202.927/2019, # E-26/200.333/2023, # E-26/200.427/2023.

**Data availability** The data supporting this work are available in tables and as supplementary materials.

## Declarations

**Competing interests** The authors declare that there are no conflicts of interest.

**Ethical approval** The authors followed the ethical standards.

**Consent to participate** The authors have consent to participate.

**Consent to publish** The authors have consent to publish.

**Open Access** This article is licensed under a Creative Commons Attribution 4.0 International License, which permits use, sharing, adaptation, distribution and reproduction in any medium or format, as long as you give appropriate credit to the original author(s) and the source, provide a link to the Creative Commons licence, and indicate if changes were made. The images or other third party material in this article are included in the article’s Creative Commons licence, unless indicated otherwise in a credit line to the material. If material is not included in the article’s Creative Commons licence and your intended use is not permitted by statutory regulation or exceeds the permitted use, you will need to obtain permission directly from the copyright holder. To view a copy of this licence, visit <http://creativecommons.org/licenses/by/4.0/>.

## References

- Alexandrakis, G., Petrakis, S., & Kampanis, N. A. (2021). Integrating geomorphological data, geochronology and archaeological evidence for coastal landscape reconstruction, the case of Ammoudara Beach, Crete. *Water*, 13(9), 1269. <https://doi.org/10.3390/w13091269>
- Angulo, R. J., Lessa, G. C., & Souza, M. C. (2006). A critical review of mid- to late-Holocene sea-level fluctuations on the eastern Brazilian coastline. *Quaternary Science Reviews*, 25, 486–506. <https://doi.org/10.1016/j.quascirev.2005.03.008>
- Armstrong-Altrin, J. S., Lee, Y. I., Kasper-Zubillaga, J. J., & Trejo-Ramírez, E. (2017). Mineralogy and geochemistry of sands along the Manzanillo and El Carrizal beach areas, southern Mexico: Implications for paleoweathering, provenance and tectonic setting. *Geological Journal*, 52, 559–582. <https://doi.org/10.1002/gj.2792>
- Arz, H. W., Pätzold, J., & Wefer, G. (1998). Correlated millennial-scale changes in surface hydrography and terrigenous sediment yield inferred from last-glacial marine deposits off Northeastern Brazil. *Quaternary Research*, 50(2), 157–166. <https://doi.org/10.1006/qres.1998.1992>

- Baker, P. A., Seltzer, G. O., Fritz, S. C., et al. (2001). The history of South American tropical precipitation for the past 25,000 years. *Science*, *291*, 640.
- Behling, H. (1995). A high resolution Holocene pollen record from Lago do Pires, SE Brazil: Vegetation, climate and fire history. *Journal of Paleolimnology*, *14*, 253–268. <https://doi.org/10.1007/BF00682427>
- Bela, V. A., Bessa, A. Z., Armstrong-Altrin, J. S., Kamani, F. A., Nya, E. D. B., & Nguetchoua, G. (2023). Provenance of clastic sediments: A case study from Cameroon, Central Africa. *Solid Earth Sciences*, *8*(2), 105–122. <https://doi.org/10.1016/j.sesci.2023.03.002>
- Berger, A., & Loutre, M.-F. (1991). Insolation values for the climate of the last 10 million years. *Quaternary Science Reviews*, *10*, 297–317. [https://doi.org/10.1016/0277-3791\(91\)90033-Q](https://doi.org/10.1016/0277-3791(91)90033-Q)
- Bhatia, M. R., & Crook, K. A. W. (1986). Trace element characteristics of graywackes and tectonic setting discrimination of sedimentary basins. *Contributions to Mineralogy and Petrology*, *92*, 181–193.
- Bouillon, S., Connolly, R. M., & Lee, S. Y. (2008). Organic matter exchange and cycling in mangrove ecosystems: Recent insights from stable isotope studies. *Journal of Sea Research*, *59*(1–2), 44–58. <https://doi.org/10.1016/j.seares.2007.05.001>
- Bronk Ramsey, C. (2009). Bayesian analysis of radiocarbon dates. *Radiocarbon*, *51*(1), 337–360.
- Brooks, P. D., Haas, P. A., & Huth, A. K. (2007). Seasonal variability in the concentration and flux of organic matter and inorganic nitrogen in a semiarid catchment, San Pedro River, Arizona. *Journal of Geophysical Research*, *112*, G03S04. <https://doi.org/10.1029/2006JG00275>
- Cao, J., Wu, M., Chen, Y., Hu, K., Bian, L., Wang, L., & Zhang, Y. (2012). Trace and rare earth element geochemistry of Jurassic mudstone in the northern Qaidam Basin, northwest China. *Chemie Der Erde*, *72*, 245–252. <https://doi.org/10.1016/j.chemer.2011.12.002>
- Carneiro, L. M., Zucchi, M. R., Jesus, T. B., Silva Júnior, J. B., & Hadlich, G. M. (2021).  $\delta^{13}\text{C}$ ,  $\delta^{15}\text{N}$  and TOC/TN as indicators of the origin of organic matter in sediment samples from the estuary of a tropical river. *Marine Pollution Bulletin*, *172*, 112857. <https://doi.org/10.1016/j.marpolbul.2021.112857>
- Carvalho, B. C., Dalbosco, A. L. P., & Guerra, J. V. (2020). Shoreline position change and the relationship to annual and interannual meteorological conditions in Southeastern Brazil. *Estuarine, Coastal and Shelf Science*, *235*, 106582. <https://doi.org/10.1016/j.ecss.2020.106582>
- Carvalho, B. C., & Guerra, J. V. (2020). Aplicação de modelo de tendência direcional de transporte ao longo de uma ilha-barreira: Restinga da Marambaia RJ, SE Brasil. *Anuário Do Instituto De Geociências-UFRJ*, *43*, 101–118.
- Castelo, W. F. L., Martins, M. V. A., Martínez-Colón, M., et al. (2021). Disentangling natural vs. anthropogenic induced environmental variability during the Holocene: Marambaia Cove, SW sector of the Sepetiba Bay (SE Brazil). *Environmental Science and Pollution Research*, *28*, 22612–22640. <https://doi.org/10.1007/s11356-020-12179-9>
- Chen, J., & Strous, M. (2013). Denitrification and aerobic respiration, hybrid electron transport chains and co-evolution. *Biochimica Et Biophysica Acta BBA-Bioenergetics*, *1827*(2), 136–144. <https://doi.org/10.1016/j.bbabi.2012.10.002>
- Cox, R., Lowe, D. R., & Cullers, R. L. (1995). The influence of sediment recycling and basement composition of evolution of mudrock chemistry in the southwestern United States. *Geochimica Et Cosmochimica Acta*, *59*, 2919–2940. [https://doi.org/10.1016/0016-7037\(95\)00185-9](https://doi.org/10.1016/0016-7037(95)00185-9)
- CPRM. (2001). *Serviço Geológico do Brasil. Geologia do Estado do Rio de Janeiro* (p. 614). Brasília. Retrieved December 2023, from [https://rigeo.cprm.gov.br/jspui/bitstream/doc/17229/4/rele\\_proj\\_rj\\_geologia.pdf](https://rigeo.cprm.gov.br/jspui/bitstream/doc/17229/4/rele_proj_rj_geologia.pdf)
- Cruz, F. W., Burns, S. J., Karmann, I., et al. (2005). Insolation-driven changes in atmospheric circulation over the past 116,000 years in subtropical Brazil. *Nature*, *434*, 63–66.
- Cullers, R. L. (2002). Implications of elemental concentrations for provenance, redox conditions, and metamorphic studies of shales and limestones near Pueblo, CO, USA. *Chemical Geology*, *191*(4), 305–327. [https://doi.org/10.1016/S0009-2541\(02\)00133-X](https://doi.org/10.1016/S0009-2541(02)00133-X)
- Dadalto, T. P., Carvalho, B. C., Guerra, J. V., Reis, A. T., & Silva, C. G. (2022). Holocene morpho-sedimentary evolution of Marambaia Barrier Island SE Brazil. *Quaternary Research*, *105*, 182–200. <https://doi.org/10.1017/qua.2021.43>
- Davies, J. L. (1980). *Geographic variation in coastal development*. Longman.
- Deines, P. (1980). The isotopic composition of reduced organic carbon. In P. Fritz & J. C. H. Fontes (Eds.), *Amsterdam: Handbook of environmental isotope geochemistry* (Vol. 1, pp. 329–406). Elsevier Scientific Publishing Company. <https://doi.org/10.1016/b978-0-444-41780-0.50015-8>
- Deng, H. W., & Qian, K. (1993). *Analysis of sedimentary geochemistry and environment*. Science Technology Press.
- Dress, L. R., & Wilding, L. P. (1973). Elemental variability within a sampling unit. *Soil Science Society American Proceedings*, *37*, 82–87.
- Fedo, C. M., Nesbitt, H. W., & Young, G. M. (1995). Unraveling the effects of potassium metasomatism in sedimentary rocks and paleosols, with implications for paleoweathering conditions and provenance. *Geology*, *23*(10), 921–924. [https://doi.org/10.1130/0091-7613\(1995\)023%3c0921:UTEOPM%3e2.3.CO;2](https://doi.org/10.1130/0091-7613(1995)023%3c0921:UTEOPM%3e2.3.CO;2)
- Fitzpatrick, R. W., & Chittleborough, D. J. (2002). Titanium and zirconium minerals. In J. B. Dixon & D. G. Schulze (Eds.), *Minerals in soil environments* (Chapter 22, pp. 667–690). Soil Science Society of America. <https://doi.org/10.2136/sssabookser7.c22>
- Folk, R. L., & Ward, W. C. (1957). Brazos River bar: A study in the significance of grain size parameters. *Journal of Sedimentary Petrology*, *27*(1), 3–26.
- Freudenthal, T., Wagner, T., Wenzhöfer, F., Zabel, M., & Wefer, G. (2001). Early diagenesis of organic matter from sediments of the eastern subtropical Atlantic: Evidence from stable nitrogen and carbon isotopes. *Geochimica Et Cosmochimica Acta*, *65*(11), 1795–1808. <https://doi.org/10.1016/S0016-70370100554-3>
- Friederichs, Y. L., Reis, A. T., Silva, C. G., Toulemonde, B., Maia, R. M. C., & Guerra, J. V. (2013). Arquitetura sísmica do sistema fluvio-estuarino da Baía de Sepetiba preservado na estratigrafia rasa da plataforma adjacente, Rio de Janeiro, Brasil. *Brazilian Journal of Geology*, *43*(1), 998–1012.
- Fu, X., Wang, J., Chen, W., Feng, X., Wang, D., Song, C., & Zeng, S. (2015). Elemental geochemistry of the early Jurassic black shales in the Qiangtang Basin, eastern Tethys: Constraints for palaeoenvironment conditions. *Geological Journal*, *513*, 443–454. <https://doi.org/10.1002/gj.2642>
- Galloway, W. E., & Hobday, D. K. (1983). *Terrigenous clastic depositional systems* (p. 489). Springer.
- Goldich, S. S. (1938). A study of rock weathering. *Journal of Geology*, *46*, 17–58. <https://doi.org/10.1086/624619>
- Govin, A., Holzwarth, U., Heslop, D., Keeling, L. F., Zabel, M., Mulitza, S., Collins, J. A., & Chiessi, C. M. (2012). Distribution of major elements in Atlantic surface sediments 36°N–49°S: Imprint of terrigenous input and continental weathering. *Geochemistry, Geophysics, Geosystems*, *13*(1). <https://doi.org/10.1029/2011GC003785>
- Hay, W. W. (1998). Detrital sediment fluxes from continents to oceans. *Chemical Geology*, *145*–4, 287–323. <https://doi.org/10.1016/S0009-25419700149-6>









- Heaton, T. H. E. (1986). Isotopic studies of nitrogen pollution in the hydrosphere and atmosphere: A review. *Chemical Geology: Isotope Geoscience*, 59, 87–102. [https://doi.org/10.1016/0168-9622\(86\)90059-X](https://doi.org/10.1016/0168-9622(86)90059-X)
- Heaton, T., Köhler, P., Butzin, M., Bard, E., Reimer, R., Austin, W., & Skinner, L. (2020). Marine 20—The marine radiocarbon age calibration curve 0–55,000 cal BP. *Radiocarbon*, 62(4), 779–820. <https://doi.org/10.1017/RDC.2020.68>
- Heilbron, M., Eirado, L.G., & Almeida, J. (2016a). Geologia e recursos minerais do Estado do Rio de Janeiro. Programa Geologia do Brasil, integração, atualização e difusão de Dados da geologia do Brasil, Mapas geológicos Estaduais, Escala 1:400.000. Ministério de Minas e Energia, CPRM.
- Heilbron, M., & Machado, N. (2003). Timing of terrane accretion in the Neoproterozoic-Eopaleozoic Ribeira Orangen SE, Brazil. *Precambrian Research*, 125(1–2), 87–112. <https://doi.org/10.1016/S0301-92680300082-2>
- Heilbron, M., Mohriak, W., Valeriano, C.M., Milani, E., Almeida, J. C. H., & Tupinambá, M. (2000). From collision to extension: The roots of the Southeastern continental margin of Brazil. In M. T. Mohriak (Ed.), *Atlantic rifts and continental margin. AGU geophysical monograph series* (Vol. 115, 354 pp).
- Heilbron, M., Ribeiro, A., Valeriano, C. M., Paciullo, F. V., Almeida, J. C. H., Trouw, R. J. A., et al. (2016b). The Ribeira Belt. In M. Heilbron, U. Cordani, & F. Alkmim (Eds.), *São Francisco Craton, Eastern Brazil*. Regional geology reviews. Springer. [https://doi.org/10.1007/978-3-319-01715-0\\_15](https://doi.org/10.1007/978-3-319-01715-0_15)
- Heilbron, M., Valeriano, C., Tassinari, C. C. G., Almeida, J. C. H., Tupinambá, M., Siga, O., & Trouw, R. (2008). Correlation of Neoproterozoic terranes between the Ribeira Belt, SE Brazil and its African counterpart: Comparative tectonic evolution and open questions. *London, Geological Society, Special Publications*, 294, 211–237. <https://doi.org/10.1144/SP294.12>
- Heilbron, M., Valeriano, C. M., Peixoto, C., Tupinambá, M., Neubauer, F., Dussin, I., Corrales, F., Bruno, H., Lobato, M., Almeida, J. C. H., & Silva, L. G. E. (2020). Neoproterozoic magmatic arc systems of the central Ribeira belt, SE-Brazil, in the context of the West-Gondwana pre-collisional history: A review. *Journal of South American Earth Sciences*, 103, 102710. <https://doi.org/10.1016/j.jsames.2020.102710>
- Hesp, P. A., & Short, A. D. (1999). Barrier morphodynamics. In A. D. Short (Ed.), *Handbook of beach and shoreface morphodynamics* (pp. 307–333). John Wiley & Sons.
- Hiscott, R. N. (1984). Ophiolitic source rocks for Taconic-age flysch: Trace-element evidence. *Geological Society of America Bulletin*, 95(11), 1261–1267. [https://doi.org/10.1130/0016-7606\(1984\)95%3c1261:OSRFTF%3e2.0.CO;2](https://doi.org/10.1130/0016-7606(1984)95%3c1261:OSRFTF%3e2.0.CO;2)
- Ho, H. H., Swennen, R., & Van Damme, A. (2010). Distribution and contamination status of heavy metals in estuarine sediments near Cua Ong Harbor, Ha Long Bay, Vietnam. *Geologica Belgica*, 13(1–2), 37–47.
- Hogg, A., Heaton, T., Hua, Q., Palmer, J., Turney, C., Southon, J., et al. (2020). SHCal20 southern hemisphere calibration, 0–55,000 years cal BP. *Radiocarbon*, 62(4), 759–778. <https://doi.org/10.1017/RDC.2020.59>
- Idier, D., Bertin, X., Thompson, P., & Pickering, M. D. (2019). Interactions between mean sea level, tide, surge, waves and flooding: Mechanisms and contributions to sea level variations at the coast. *Surveys in Geophysics*, 40, 1603–1630. <https://doi.org/10.1007/s10712-019-09549-5>
- Jones, B., & Manning, D. A. C. (1994). Comparison of geochemical indices used for the interpretation of palaeoredox conditions in ancient mudstones. *Chemical Geology*, 111(1–4), 111–129. [https://doi.org/10.1016/0009-2541\(94\)90085-X](https://doi.org/10.1016/0009-2541(94)90085-X)
- Kendall, C., Silva, S. R., & Kelly, V. J. (2001). Carbon and nitrogen isotopic compositions of particulate organic matter in four large river systems across the United States. *Hydrological Processes*, 15(7), 1301–1346. <https://doi.org/10.1002/hyp.216>
- Kim, G., Yang, H. S., & Church, T. M. (1999). Geochemistry of alkaline earth elements Mg, Ca, Sr, Ba in the surface sediments of the Yellow Sea. *Chemical Geology*, 153(1–4), 1–10. [https://doi.org/10.1016/S0009-2541\(98\)00149-1](https://doi.org/10.1016/S0009-2541(98)00149-1)
- Koinig, K. A., Shoty, W., Lotter, A. F., Ohlendorf, C., & Sturm, M. (2003). 9000 years of geochemical evolution of lithogenic major and trace elements in the sediment of an alpine lake—The role of climate, vegetation, and land-use history. *Journal of Paleolimnology*, 30, 307–320. <https://doi.org/10.1023/A:1026080712312>
- Kraft, J. C., & John, C. J. (1979). Lateral and vertical facies relations of transgressive barrier. *AAPG*, 63, 2145–2163. <https://doi.org/10.1306/2F9188F6-16CE-11D7-8645000102C1865D>
- Kryc, K. A., Murray, R. W., & Murray, D. W. (2003). Al-to-oxide and Ti-to-organic linkages in biogenic sediment: Relationships to paleo-export production and bulk Al/Ti. *Earth and Planetary Science Letters*, 211(1–2), 125–141. [https://doi.org/10.1016/S0012-821X\(03\)00136-5](https://doi.org/10.1016/S0012-821X(03)00136-5)
- Laignel, B., Vignudelli, S., Almar, R., Becker, M., Bentamy, A., Benveniste, J., Birol, F., Frappart, F., Idier, D., Salameh, E., Passaro, M., Menende, M., Simard, M., Turki, E. I., & Verpoorter, C. (2023). Observation of the coastal areas, estuaries and deltas from space. *Surveys in Geophysics*, 1–48. <https://doi.org/10.1007/s10712-022-09757-6>
- Lambeck, K., Rouby, H., Purcell, A., Sun, Y., & Sambridge, M. (2014). Sea level and global ice volumes from the Last Glacial Maximum to the Holocene. *PNAS*, 111(43), 5296–15303.
- Ledru, M. P. (1993). Late Quaternary environmental and climatic changes in central Brazil. *Quaternary Research*, 39, 90–98.
- Li, Y., Zhang, H., Tu, C., Fu, C., Xue, Y., & Luo, Y. (2016). Sources and fate of organic carbon and nitrogen from land to ocean: Identified by coupling stable isotopes with C/N ratio. *Estuarine Coastal Shelf Science*, 181, 114–122.
- Lin, G., & Sternberg, L. S. L. (1992). Differences in morphology, carbon isotope ratios, and photosynthesis between scrub and fringe mangroves in Florida, USA. *Aquatic Botany*, 42, 303–313.
- Liu, B. J. (1980). *Sedimentary Petrology*. Geological Press.
- Liu, Y. J., Cao, L. M., Li, Z. L., Wang, H. N., Chu, T. Q., & Zhang, Z. R. (1984). *Element geochemistry*. Science Press.
- Macario, K., Alves, E., Belém, A., Aguilera, O., Bertucci, T., Tenório, M., & Caon, J. (2018). The marine reservoir effect on the coast of Rio de Janeiro: Deriving  $\Delta R$  values from fish otoliths and mollusk shells. *Radiocarbon*, 60(4), 1151–1168. <https://doi.org/10.1017/RDC.2018.23>
- Martins, J. M. A., Silva, T. S. M., Femande, A. M., Massone, C. G., & Carreira, R. S. (2016). Characterization of particulate organic matter in a Guanabara Bay-coastal ocean transect using elemental, isotopic and molecular markers. *Pan-American Journal of Aquatic Sciences*, 11(4), 276–291.
- McArthur, J. M., Tyson, R. V., Thomson, J., & Matthey, D. (1992). Early diagenesis of marine organic matter: Alteration of the carbon isotopic composition. *Marine Geology*, 105(1–4), 51–61. [https://doi.org/10.1016/0025-3227\(92\)90181-G](https://doi.org/10.1016/0025-3227(92)90181-G)
- McLennan, S. M., Hemming, S., McDaniel, D. K., Hanson, G. M. (1993). Geochemical approaches to sedimentation, provenance, and tectonics. In M. J. Johnsson & A. Basu (Eds.), *Processes controlling the composition of clastic sediments. Special Papers* (Vol. 284, pp. 21–40). Geological Society of America
- Meyers, P. A. (2003). Applications of organic geochemistry to paleolimnological reconstructions: A summary of examples from the Laurentian Great Lakes. *Organic Geochemistry*, 34(2), 261–289. [https://doi.org/10.1016/S0146-6380\(02\)00168-7](https://doi.org/10.1016/S0146-6380(02)00168-7)
- Meyers, P. A., & Ishiwatari, R. (1993). Lacustrine organic geochemistry—An overview of indicators of organic matter sources and

- diagenesis in lake sediments. *Organic Geochemistry*, 207, 867–900. <https://doi.org/10.1016/0146-63809390100-P>
- Montibeller, C. C., Zanardo, A., & Navarro, G. R. B. (2017). Decifrando a proveniência dos folhelhos da formação Ponta Grossa na região de Rio Verde de Mato Grosso e Coxim MS através de métodos petrográficos e geoquímicos. *Geologia USP. Série Científica*, 171, 41–59. <https://doi.org/10.11606/issn.2316-9095.v17-294>
- Mota, C. E. M. (2012). Petrogênese e geocronologia das intrusões alcalinas de Morro Redondo, Mendanha e Morro de São João: caracterização do magmatismo alcalino no estado do Rio de Janeiro e implicações geodinâmicas. Tese (Doutorado em Geologia) – Universidade do Estado do Rio de Janeiro, Rio de Janeiro
- Moterani, A. C. M., Júnior, R. P., Geraldês, M. C., & Martins, M. V. A. (2020). Magmatismo pós-tectônico investigado por meio dos métodos geocronológicos U-Pb e Lu-Hf, complexo Pedra Branca, Rio de Janeiro–RJ. *Geociências*, 3904, 903–923.
- Nakatsuka, T., Watanabe, K., Handa, N., Matsumoto, E., & Wada, E. (1995). Glacial to interglacial surface nutrient variations of Bering deep basins recorded by  $\delta^{13}\text{C}$  and  $\delta^{15}\text{N}$  of sedimentary organic matter. *Paleoceanography*, 10, 1047–1061. <https://doi.org/10.1029/95PA02644>
- Nesbitt, H. W., & Young, G. M. (1982). Early Proterozoic climates and plate motions inferred from major element chemistry of lutites. *Nature*, 299, 715–717. <https://doi.org/10.1038/299715a010.1038/299715a0>
- Nesbitt, H. W., & Young, G. M. (1984). Prediction of some weathering trends of plutonic and volcanic rocks based on thermodynamic and kinetic considerations. *Geochimica Et Cosmochimica Acta*, 48(7), 1523–1534. [https://doi.org/10.1016/0016-7037\(84\)90408-3](https://doi.org/10.1016/0016-7037(84)90408-3)
- Ngueutchoua, G., Bessa, A. Z. E., Eyong, J. T., Zandjio, D. D., Djaoro, H. B., & Nfada, L. T. (2019). Geochemistry of cretaceous fine-grained siliciclastic rocks from Upper Mundek and Logbadjeck Formations, Douala sub-basin, SW Cameroon: Implications for weathering intensity, provenance, paleoclimate, redox condition, and tectonic setting. *Journal of African Earth Sciences*, 152, 215–236. <https://doi.org/10.1016/j.jafrearsci.2019.02.021>
- Noori, B., Ghadimvand, N. K., Movahed, B., & Yousefpour, M. (2016). Sedimentology and depositional environment of the Kazhdumi Formation Sandstones in the northwestern area of the Persian Gulf. *Open Journal of Geology*, 6, 1401–1422.
- Oertel, G.F. (1985). The barrier island system. In G. F. Oertel, S. P. Leatherman (Eds.), *Barrier islands*. *Marine Geology*, 63(1–4), 1–18. [https://doi.org/10.1016/0025-3227\(85\)90077-5](https://doi.org/10.1016/0025-3227(85)90077-5)
- Okunlola, O. A., & Idowu, O. (2012). The geochemistry of claystone-shale deposits from the Maastrichtian Patti formation, Southern Bida basin, Nigeria. *Earth Sciences Research Journal*, 16, 139–150.
- Peixoto, C., Heilbron, M., Ragatky, D., Armstrong, R., Dantas, E., Valeriano, C., & Simonetti, A. (2017). Tectonic evolution of the Juvenile Tonian Serra da Prata magmatic arc in the Ribeira belt, SE Brazil: Implications for early west Gondwana amalgamation. *Precambrian Research*, 302, 221–254. <https://doi.org/10.1016/j.precamres.2017.09.017>
- Porto, R., Jr., Tesser, L. R., & Duarte, B. P. (2018). A origem do acamamento magmático no granito Pedra Branca, Maciço da Pedra Branca, Rio de Janeiro, Brasil. São Paulo, UNESP. *Geociências*, 37(2), 237–251.
- Powell, W. G., Johnston, P. A., & Collom, C. J. (2003). Geochemical evidence for oxygenated bottom waters during deposition of fossiliferous strata of the Burgess Shale Formation. *Palaeogeography, Palaeoclimatology, Palaeoecology*, 201(3–4), 249–268. <https://doi.org/10.1016/S0031-01820300612-6>
- Prahl, F. G., Lange, G. J., Scholten, S., & Cowie, G. L. (1997). A case of post-depositional aerobic degradation of terrestrial organic matter in turbidite deposits from the Madeira Abyssal Plain. *Organic Geochemistry*, 27, 141–152. [https://doi.org/10.1016/S0146-6380\(97\)00078-8](https://doi.org/10.1016/S0146-6380(97)00078-8)
- Reimann, L., Vafeidis, A., & Honsel, L. (2023). Population development as a driver of coastal risk: Current trends and future pathways. *Cambridge Prisms: Coastal Futures*, 1, E14. <https://doi.org/10.1017/cft.2023.3>
- Reis, A. T., Amendola, G., Dadalto, T. P., Silva, C. G., Tardin Poço, R., Guerra, J. V., Martins, V., Cardia, R. R., Gorini, C., & Rabineau, M. (2020). Arquitetura e Evolução Depositional da Sucessão Sedimentar Pleistoceno Tardio-Holoceno Últimos ~20 Ka da Baía de Sepetiba RJ. São Paulo, UNESP. *Geociências*, 39(3), 695–708.
- Rimmer, S. M. (2004). Geochemical paleoredox indicators in Devonian-Mississippian black shales, Central Appalachian Basin USA. *Chemical Geology*, 206(3–4), 373–391. <https://doi.org/10.1016/j.chemgeo.2003.12.029>
- Rodelli, M. R., Gearing, J. N., Gearing, P. J., Marshall, N., & Sasekumar, A. (1984). Stable isotope ratios as a tracer of mangrove carbon in Malaysian ecosystems. *Oecologia*, 61, 326–333. <https://doi.org/10.1007/BF00379629>
- Rodriguez, A. B., Anderson, J. B., & Simms, A. R. (2005). Terrace inundation as an autocyclic mechanism for parasequence formation: Galveston Estuary, Texas, U.S.A. *Journal of Sedimentary Research*, 75(4), 608–620. <https://doi.org/10.2110/jsr.2005.050>
- Roy, P. S., Cowell, P. J., Ferland, M. A., & Thom, B. G. (1994). Wave-dominated coasts. In R. W. G. Carter & C. D. Woodroffe (Eds.), *Coastal evolution, late Quaternary shoreline morphodynamics* (pp. 121–186). Cambridge University Press.
- Salgado-Labouriau, M. L., Barberi, M., Ferraz Vicentini, K. R., & Parizzi, M. G. (1998). A dry climatic event during the late Quaternary of tropical Brazil. *Review of Palaeobotany and Palynology*, 99, 115–129.
- Sampaio, L., Freitas, R., Máguas, C., Rodrigues, A., & Quintino, V. (2010). Coastal sediments under the influence of multiple organic enrichment sources: An evaluation using carbon and nitrogen stable isotopes. *Marine Pollution Bulletin*, 60(2), 272–282. <https://doi.org/10.1016/j.marpolbul.2009.09.008>
- Saucedo-Ramírez, O. A., Mahlknecht, J., & González-Bravo, R. (2022). Optimization of water allocation networks in highly engineered basins: The case of Guandu River basin, Rio de Janeiro State, Brazil. *Journal of Cleaner Production*, 358, 131787. <https://doi.org/10.1016/j.jclepro.2022.131787>
- Servant, M., Soubies, E., Suguio, K., Turcq, B., & Foutnier, M. (1989). Alluvial fans in southeastern Brazil as an evidence for early Holocene dry climate period. In *International symposium on global changes in South America during the Quaternary*, São Paulo (Brazil), pp. 75–80.
- Shao, J., Yang, S., & Li, C. (2012). Chemical indices CIA and WIP as proxies for integrated chemical weathering in China: Inferences from analysis of fluvial sediments. *Sedimentary Geology*, 265–266, 110–120. <https://doi.org/10.1016/j.sedgeo.2012.03.020>
- Shapleigh, J. P. (2013). Denitrifying prokaryotes. In E. Rosenberg, E. F. DeLong, S. Lory, E. Stackebrandt, & F. Thompson (Eds.), *The prokaryotes* (pp. 405–425). Springer. [https://doi.org/10.1007/978-3-642-30141-4\\_71](https://doi.org/10.1007/978-3-642-30141-4_71)
- Silva, L. C., Alves Martins, M. V., Castelo, W. F. L., Saibro, M. B., Rangel, D., Pereira, E., Bergamaschi, S., Sousa, S. H. M., Varela, J., Laut, L., Frontalini, F., Chaves, H., Reis, A. T., Aguilera, O., Zauboub, N., Cheriyan, E., & Geraldês, M. C. (2022). Trace metals enrichment and Potential Ecological Risk in sediments of the Sepetiba Bay Rio de Janeiro, SE Brazil. *Marine Pollution Bulletin*, 177, 113485. <https://doi.org/10.1016/j.marpolbul.2022.113485>
- Skrabal, S. A. (1995). Distributions of dissolved titanium in Chesapeake Bay and the Amazon River Estuary. *Geochimica Et*

- Cosmochimica Acta*, 59, 2449–2458. [https://doi.org/10.1016/0016-7037\(95\)00139-5](https://doi.org/10.1016/0016-7037(95)00139-5)
- Smith, B. N., & Epstein, S. (1971). Two categories of  $^{13}\text{C}/^{12}\text{C}$  ratios for higher plants. *Plant Physiology*, 47, 380–384.
- Suguio, K., Turcq, B., Servant, M., Soubis, E. & Fournier, M. (1989). Holocene fluvial deposits in southeastern Brazil: Chronology and palaeohydrological implications. In *International symposium on global changes in South America during the Quaternary*, São Paulo (Brazil), pp. 70–73.
- Sweeney, R. E., & Kaplan, I. R. (1980). Natural abundances of  $^{15}\text{N}$  as a source indicator for near-shore marine sedimentary and dissolved nitrogen. *Marine Chemistry*, 92(2), 81–94. [https://doi.org/10.1016/0304-4203\(80\)90062-6](https://doi.org/10.1016/0304-4203(80)90062-6)
- Tabatabaei, H., Motamed, A., Soleimani, B., & Kamali, M. R. (2012). Geochemistry of Gurpi-Pabdeh-Asmari formations and its implication on chemical variation during deposition of Pabdeh Formation, Zagros Basin. *Himalayan Geology*, 33(2), 126–138.
- Taboada, T., Cortizas, A. M., Garcia, C., & Garcia-Rodeja, E. (2006). Particle-size fractionation of titanium and zirconium during weathering and pedogenesis of granitic rocks in NW Spain. *Geoderma*, 131, 218–236. <https://doi.org/10.1016/j.geoderma.2005.03.025>
- Tupinambá, M., Heilbron, M., Duarte, B. P., Nogueira, J. R., Valladares, C. S., Almeida, J. C. H., Eirado, L. G., Medeiros, S. R., Almeida, C. G., Miranda, A. W. A., & Ragatky, C. D. (2007). Geologia da Faixa Ribeira Setentrional: Estado da Arte e Conexões com a Faixa Araçuaí. *Geonomos*, 15, 67–79.
- Tupinambá, M., Heilbron, M., Valeriano, C., Porto, R., Jr., Dios, F. B., Machado, N., Silva, L. G. E., & Almeida, J. C. H. (2012). Juvenile contribution of the Neoproterozoic Rio Negro Magmatic Arc Ribeira Belt, Brazil: Implications for Western Gondwana amalgamation. *Gondwana Research*, 21, 422–438. <https://doi.org/10.1016/j.gr.2011.05.012>
- Tupinambá, M., Teixeira, W., & Heilbron, M. (2000). Neoproterozoic western Gondwana assembly and subduction-related plutonism: The role of the Rio Negro Complex in the Ribeira Belt, southeastern Brazil. *Revista Brasileira De Geociências, Rio De Janeiro*, 30(1), 7–11.
- Valeriano, C. M., Mendes, J. C., Tupinambá, M., Bongioio, E., Heilbron, M., & Junho, M. C. B. (2016). Cambro-Ordovician post-collisional granites of the Ribeira Belt, SE-Brasil: A case of terminal magmatism of a hot orogen. *Journal of South American Earth Sciences*, 68, 269–281. <https://doi.org/10.1016/j.jsames.2015.12.014>
- Valeriano, C. M., Tupinambá, M., Simonetti, A., Heilbron, M., Almeida, J. C. H., & Eirado, L. G. (2011). U-Pb LA-MC-ICP-MS geochronology of Cambro-Ordovician post-collisional granites of the Ribeira belt, southeast Brazil: Terminal Brasiliano magmatism in central Gondwana supercontinent. *Journal of South American Earth Sciences*, 32, 416–428. <https://doi.org/10.1016/j.jsames.2011.03.003>
- Vizzini, S., Savona, B., Caruso, M., Savona, A., & Mazzola, A. (2005). Analysis of stable carbon and nitrogen isotopes as a tool for assessing the environmental impact of aquaculture: A case study from the western Mediterranean. *Aquaculture International*, 13, 157–165. <https://doi.org/10.1007/s10499-004-9023-5>
- Walling, D. E. (2006). Human impact on land–ocean sediment transfer by the world’s rivers. *Geomorphology*, 79, 192–216. <https://doi.org/10.1016/j.geomorph.2006.06.019>
- Wang, A. (1996). Discriminant effect of sedimentary environment by the Sr/Ba ratio of different existing forms. *Acta Sedimentologica Sinica*, 14, 168–173.
- Wang, A., Wang, Z., Liu, J., Xu, N., & Li, H. (2021). The Sr/Ba ratio response to salinity in clastic sediments of the Yangtze River Delta. *Chemical Geology*, 559, 119–923. <https://doi.org/10.1016/j.chemgeo.2020.119923>
- Wang, M., Nuamah, L. A., Zhang, Y., & Huang, J. Y. (2014). Variability in  $\delta^{13}\text{C}$  and  $\delta^{15}\text{N}$  stable isotope signatures in mangrove ecosystem of Hainan, China. *Advanced Materials Research*, 1073–1076, 535–540. <https://doi.org/10.4028/www.scientific.net/amr.1073-1076.535>
- Wang, X.-C., Chen, R. F., & Gardner, G. B. (2004). Sources and transport of dissolved and particulate organic carbon in the Mississippi River estuary and adjacent coastal waters of the northern Gulf of Mexico. *Marine Chemistry*, 89(1–4), 241–256. <https://doi.org/10.1016/j.marchem.2004.02.014>
- Wedepohl, K. H. (1969). Composition and abundance of common igneous rocks. In K. H. Wedepohl (Ed.), *Handbook of geochemistry* (Vol. 1, pp. 227–249). Springer-Verlag.
- Wei, W., & Algeo, T. J. (2020). Elemental proxies for paleosalinity analysis of ancient shales and mudrocks. *Geochimica Et Cosmochimica Acta*, 287, 341–366. <https://doi.org/10.1016/j.gca.2019.06.034>
- Whitney, B. S., & Mayle, F. E. (2012). Pediastrum species as potential indicators of lake-level change in tropical South America. *Journal of Paleolimnology*, 47, 601–615. <https://doi.org/10.1007/s10933-012-9583-8>
- Xu, B., Ding, S., Wang, Y., & Liu, Q. (2011). Geochemical characteristics of illite clay rocks from the Shihezi Formation in the Hanxing mining area and its sedimentary environment. *Mining Science and Technology*, 214, 495–500.
- Yan, K., Wang, C. L., Mischke, S., Wang, J. Y., Shen, L. J., Yu, X. C., & Meng, L. Y. (2021). Major and trace-element geochemistry of Late Cretaceous clastic rocks in the Jitai Basin, southeast China. *Scientific Reports*, 111, 13846. <https://doi.org/10.1038/s41598-021-93125-8>
- Ye, F., Guo, W., Shi, Z., Jia, G., & Wei, G. (2017). Seasonal dynamics of particulate organic matter and its response to flooding in the Pearl River Estuary, China, revealed by stable isotope  $\delta^{13}\text{C}$  and  $\delta^{15}\text{N}$  analyses. *JGR Oceans*, 122, 6835–6856. <https://doi.org/10.1002/2017JC012931>
- Zhao, Z. Y., Zhao, J. H., Wang, H. J., Liao, J. D., & Liu, C. M. (2007). Distribution characteristics and applications of trace elements in Junggar Basin. *Natural Gas Exploration and Development*, 30, 30–33.
- Zhou, J., & Lau, K. (1998). Does a monsoon climate exist over South America? *Journal of Climate*, 11, 1020–1040.

**Publisher's Note** Springer Nature remains neutral with regard to jurisdictional claims in published maps and institutional affiliations.

## Authors and Affiliations

Fabício Leandro Damasceno<sup>1,5</sup>  · Alves Martins Maria Virgínia<sup>1,2</sup>  · Josefa Varela Guerra<sup>3</sup>  · Antonio Tadeu dos Reis<sup>3</sup>  · Murilo Barros Saibro<sup>1</sup>  · Layla Cristine da Silva<sup>1</sup>  · Amanda Pacheco Seixas<sup>1</sup> · Vahideh Farhangi<sup>1</sup> · Karina Ferreira Chueng<sup>1</sup> · Miguel Ângelo Mane<sup>1</sup>  · Rubens Cesar Lopes Figueira<sup>4</sup>  · Mauro Galdes<sup>1</sup>

✉ Alves Martins Maria Virgínia  
virginia.martins@ua.pt

Fabício Leandro Damasceno  
fabricioldamasceno16@gmail.com

Josefa Varela Guerra  
josefa@uerj.br

Antonio Tadeu dos Reis  
tadeu.reis@gmail.com

Murilo Barros Saibro  
saibrobarros@gmail.com

Layla Cristine da Silva  
laylageologiauerj@gmail.com

Amanda Pacheco Seixas  
amapaseixas@hotmail.com

Vahideh Farhangi  
vahideh.fgi@gmail.com

Karina Ferreira Chueng  
karinachueng@yahoo.com.br

Miguel Ângelo Mane  
miguel.mane@uerj.br

Rubens Cesar Lopes Figueira  
rfigueira@usp.br

Mauro Geraldês  
mauro.geraldes@gmail.com

- <sup>1</sup> Present Address: Faculdade de Geologia, Universidade Do Estado Do Rio de Janeiro, UERJ, Av. São Francisco Xavier, 24, Sala 2020A, Maracanã, Rio de Janeiro, RJ 20550-013, Brazil
- <sup>2</sup> Departamento de Geociências, Universidade de Aveiro, GeoBioTec, Campus de Santiago, 3810-193 Aveiro, Portugal
- <sup>3</sup> Faculdade de Oceanografia, Universidade Do Estado Do Rio de Janeiro, UERJ, Rua São Francisco Xavier, 524, 4º Andar, Bloco E, Sala 4018, Rio de Janeiro, RJ CEP 20550-900, Brazil
- <sup>4</sup> Instituto Oceanográfico, Universidade de São Paulo (IOUSP), Pça. Do Oceanográfico, 191, Butantã, São Paulo 05508-120, Brazil
- <sup>5</sup> Department of Geology, Universidade Federal Fluminense, Niterói 24220-900, Brazil